

The Toroidal Obscuration of Active Galactic Nuclei

Moshe Elitzur

*Department of Physics & Astronomy, University of Kentucky
Lexington, KY 40506-0055, USA*

Abstract

Observations give strong support for the unification scheme of active galactic nuclei. The scheme is premised on toroidal obscuration of the central engine by dusty clouds that are individually very optically thick. These lectures summarize the torus properties, describe the handling and implications of its clumpy nature and present speculations about its dynamic origin.

Key words:

dust, extinction, galaxies: active, galaxies: Seyfert, infrared: general, quasars: general, radiative transfer

1 Introduction

The basic premise of the unification scheme is that every AGN is intrinsically the same object: an accreting supermassive black hole. This central engine is surrounded by a dusty toroidal structure so that the observed diversity simply reflects different viewing angles of an axisymmetric geometry. Since the torus provides anisotropic obscuration of the center, sources viewed face-on are recognized as “type 1”, those observed edge-on are “type 2”. The observational evidence for unification is covered in the lectures by C. Tadhunter and B. Peterson elsewhere in these proceedings.

A scientific theory must make falsifiable predictions, and AGN unification does meet this criterion. Unification implies that for every class of type 1 objects there is a corresponding type 2 class, therefore the theory predicts that type 2 QSO must exist. After many years of searching, the existence of QSO2 has been established, thanks to the *Sloan Digital Sky Survey*, and their spectropolarimetry even reveals the hidden type 1 nuclei at z as large as 0.6. This is a spectacular success of the unification approach. There are not that many cases

in astronomy — in fact, in all of science — where a new type of object has been predicted to exist and then actually discovered. In light of this success, it would be hard to question the basic validity of the unification approach. There is no reason, though, why the obscuring torus should be the same in every AGN; it is unrealistic to expect AGN’s to differ only in their overall luminosity but be identical in all other aspects.

The torus can be considered an acronym for Toroidal Obscuration Required by Unification Schemes. From basic considerations, Krolik & Begelman (1988) concluded that the obscuration is likely to consist of a large number of individually very optically thick dusty clouds. However, the important roll of clumpiness was not always fully appreciated, for example, its effect on AGN classification statistics: type 1 and type 2 viewing is an angle-dependent probability, not an absolute property. In these lectures I summarize the properties of the obscuring torus and try to speculate on how it might evolve with the AGN luminosity, i.e., its accretion rate. Since the main *direct* evidence for the torus comes from its IR emission, I start with a general discussion of dust emission (sec. 2). This is followed by a review of torus phenomenology (sec. 3), description of the handling of its clumpiness (sec. 4) and speculations about its dynamical origin (sec. 5).

2 Dust–Generalities

Dust grains are mixed with the gas in virtually all interstellar regions. The grains are small solid particles, built-up through collisions of many atoms (primarily Si, Mg, Al, C, O) sticking together. Grain interaction with radiation is comprised of two components: *scattering* and *absorption*; their sum is referred to as *extinction*. Scattering occurs when radiation is simply reflected off the grain surface, while during absorption the incoming photon is actually absorbed by the dust grain. The interaction of dust with radiation follows the classical theory of scattering by small geometric structures characterized by a dielectric constant. The spectral variation of the cross-section σ_λ is primarily controlled by the relation between the radiation wavelength λ and the grain size s . When $\lambda \ll s$ the grains block the radiation completely and σ_λ approaches the constant diffraction limit. When $\lambda \gg s$, σ_λ decreases as a power law. Superimposed on this general behavior are spectral features reflecting internal excitations of the grain material. Figure 1 shows the spectral behavior of each of the three cross sections for the “standard” composition of Galactic interstellar dust: 53% silicates and 47% graphite, with a grain size distribution following a power-law from $0.005\mu\text{m}$ to $0.25\mu\text{m}$ (Mathis, Rumpl, & Nordsieck, 1977). Absorption is by far the dominant process for interaction of interstellar grains with radiation in the mid- and far-IR (wavelengths longer than $\sim 2\mu\text{m}$); scattering can be safely ignored at these wavelengths.

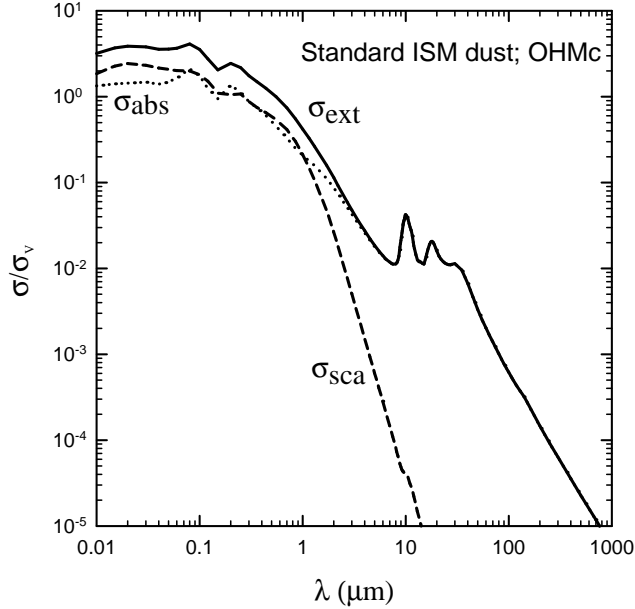


Fig. 1. Spectral shape of interstellar dust extinction coefficient and its scattering and absorption components: $\sigma_{\text{ext}} = \sigma_{\text{sca}} + \sigma_{\text{abs}}$. Standard interstellar grain mix with optical properties from Ossenkopf, Henning, & Mathis (1992) for the silicate component and Draine (2003) for the graphite.

The dust optical depth at wavelength λ is $\tau_\lambda = \int n_d \sigma_\lambda dl$, where σ_λ is the appropriate cross-section and n_d is the dust number density. The mean projected area of dust grains shows the remarkably uniform correlation $n_d \sigma_V / n_H \simeq 5 \times 10^{-22} \text{ cm}^2$, where n_H is the hydrogen density and σ_V is the dust extinction cross section at visual ($0.55 \mu\text{m}$). This ratio is approximately the same in all Galactic directions (e.g., Sparke & Gallagher, 2006). Dust obscuration with optical depth τ_V at visual therefore implies a gas column density $N_H \sim 2 \times 10^{21} \tau_V \text{ cm}^{-2}$.

2.1 Dust Temperature

The interaction of dust grains with radiation determines the state of their internal excitation; collisional energy exchange with the gas is usually negligible in the dust energy balance (although it may be important for the gas). During scattering the radiation is reflected off the grain surface and has no effect on the internal energy of the dust particle. However, when a grain absorbs an incoming photon it heats up and the energy is shared among the many internal excitation modes. In steady state, the grains must radiate away all the energy that they absorb. The balance between absorption and emission provides a condition of *radiative equilibrium*, which determines the grain temperature T : $\int \sigma_{\text{abs}\lambda} B_\lambda(T) d\lambda = \int \sigma_{\text{abs}\lambda} J_\lambda d\lambda$, where B_λ is the Planck function and $J_\lambda = \int I_\lambda d\Omega / 4\pi$ is the angle-averaged intensity. The latter can be split

into its external and diffuse components according to $J_\lambda = J_{e\lambda} + J_{\text{diff}\lambda}$. When the external radiation originates from a point source with luminosity L at a distance r , the bolometric magnitude of the external angle-averaged intensity on the illuminated surface of the dust distribution is $J_e = L/16\pi r^2$. Denote the Planck-average of the absorption coefficient $\sigma_{\text{abs}\lambda}$ by σ_{aP} and its average with the spectral shape of the external radiation by σ_{ae} . The dust temperature equation is then

$$\frac{\sigma_{\text{aP}}(T)}{\sigma_{\text{ae}}}\sigma_{\text{B}}T^4 = \frac{L}{16\pi r^2}(1 + \delta), \quad \text{where} \quad \delta = \frac{1}{\sigma_{\text{ae}}J_e} \int \sigma_{\text{abs}\lambda} J_{\text{diff}\lambda} d\lambda \quad (1)$$

and where σ_{B} is the Stefan-Boltzmann constant. The contribution of the diffuse radiation, contained in the term δ , couples this relation to the radiative transfer equation, and the dust temperature cannot be determined without solving the full dust radiative transfer problem. However, when the dust optical depth is small then the contribution of the diffuse radiation is negligible and $\delta \ll 1$. In that case eq. 1 has an immediate solution, which gives roughly $T \sim r^{-0.4}$. Dust at temperature T emits predominantly around the peak of the Planck function, $\lambda \sim 10\mu\text{m} (300\text{ K}/T)$. Because of the temperature decline with distance from the heat source, the wavelength of peak emission from distance r increases as $\sim r^{0.4}$. As the dust optical depth increases, the temperature decline becomes steeper immediately behind the illuminated surface. However, once the temperature decreases to the point that the remaining dust is optically thin at wavelengths longer than the peak of the local Planck function, the optically-thin temperature variation is recovered (see, e.g., Ivezić & Elitzur, 1997).

As the grain size increases, the roughly flat portion of the cross section evident in figure 1 extends to longer wavelengths. The result is a larger σ_{aP} and a lower grain temperature. Therefore, individual grains exposed to a heating radiation will have different temperatures, decreasing as the grain size increases, and the concept of a single “dust temperature” is meaningless. However, heating of all grains is coupled through the contribution of the diffuse radiation, and the different temperatures tend to equilibrate toward a single, common value inside sources with large optical depths. A commonly used approximation is to replace the grain mixture with a single-type composite grain whose radiative constants are constructed from the mix average. This method reproduces adequately full calculations of grain mixtures, especially when optical depths are large (e.g., Efstathiou & Rowan-Robinson, 1994; Wolf, 2003). The handling of the dust optical properties is exact in this approach, the only approximation is in replacing the temperatures of the different grain components with a single average. Wolf (2003) finds that the temperatures of different grains are within $\sim \pm 10\%$ of the temperature obtained in the mean grain approximation, and that these deviations disappear altogether when $\tau_{\text{V}} > 10$.

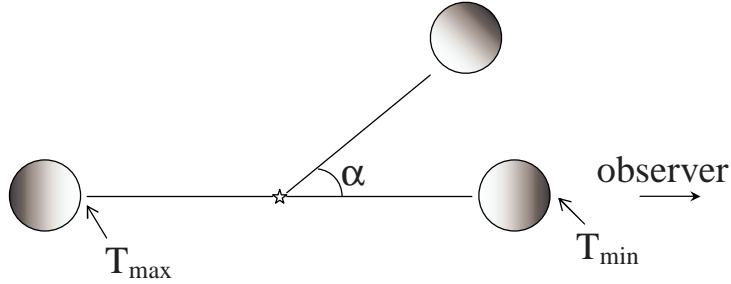


Fig. 2. The dust temperature varies on the surface of an optically thick cloud in the radiation field of an external source from T_{\max} on the illuminated face to T_{\min} on the dark side. Therefore the cloud’s IR emission is anisotropic. The visible fraction of the illuminated surface area is determined by the position angle α with respect to the observer direction.

Dust temperature distributions are profoundly different in clumpy and smooth environments. In smooth density distributions, dust temperature and distance from the radiative heating source are uniquely related to each other—given the distance, the dust temperature (either that of individual grain types or the common equilibrium value) is known, and vice versa. Clumpy media made up of discrete clouds that are individually optically thick and have dimensions that are much smaller than typical inter-cloud distances behave entirely differently. A cloud heated by a distant source will have a higher temperature on its illuminated face than on other surface areas (figure 2). The result is that in a clumpy medium, different dust temperatures coexist at the same distance from the radiation source, and the same dust temperature occurs at different distances — the dark side of a nearby cloud can be as warm as the bright side of a farther cloud. This has important implications for the IR emission from the AGN torus.

Dust grains evaporate when they become too hot. Taking $T_{\text{sub}} = 1500$ K as a typical sublimation temperature, the shortest wavelength of dust emission is $\sim 2\mu\text{m}$; emission at shorter wavelengths requires dust hotter than ~ 1500 K, thus it necessarily reflects pure scattering. Inserting the spectral shape of the nuclear UV/optical radiation from active galaxies as the heat source in eq. 1 yields the AGN dust sublimation radius

$$R_{\text{d}} \simeq 0.4 \left(\frac{L}{10^{45} \text{ erg s}^{-1}} \right)^{1/2} \left(\frac{1500 \text{ K}}{T_{\text{sub}}} \right)^{2.6} \text{ pc} \quad (2)$$

(Nenkova et al., 2008b). This value of R_{d} was determined from the temperature on the illuminated face of an optically thick dusty cloud in the composite grain approximation. In fact, larger grains are cooler and can survive closer to the heat source. The sharp boundary defined in eq. 2 is an approximation. In reality, the transition between the dusty and dust-free environments is gradual because individual components of the mix sublime at slightly different radii,

with the largest grains surviving closest to the AGN.

2.2 The 10 μ m Feature

Superimposed on the generally smooth spectral shape of the dust cross-section are two prominent features in the mid-infrared (fig. 1). They are attributed to amorphous silicate grains that produce strong opacity peaks due to the Si–O stretching and the O–Si–O bending modes centered around 10 and 18 μ m, respectively. These silicate features, especially the 10 μ m one, are visible in the observed spectral energy distribution (SED) of many astronomical objects, where they appear in either emission or absorption. This variety arises from radiative transfer effects as demonstrated in figure 3, which shows the results of exact model calculations¹.

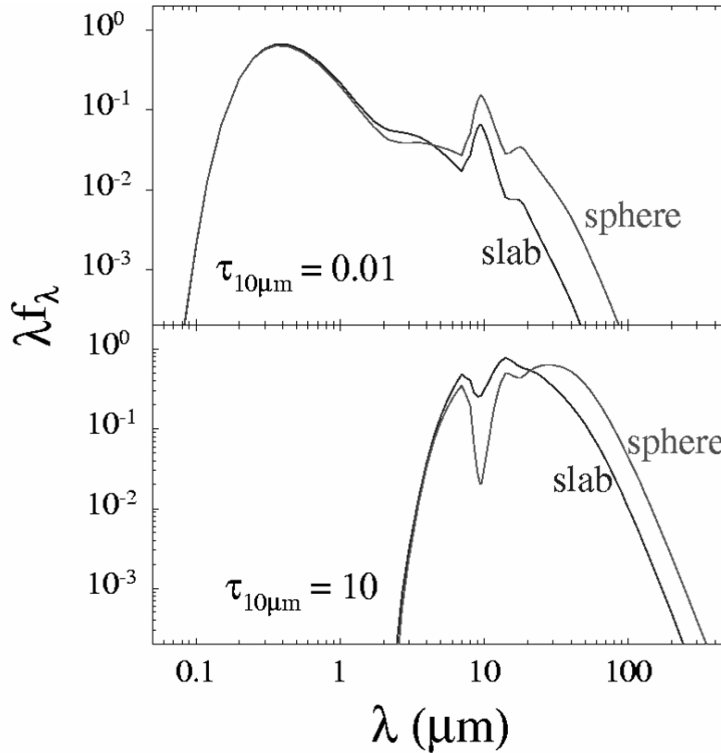


Fig. 3. Model results for dust with standard interstellar composition illuminated by black-body radiation with temperature of 10,000 K. The models labeled “sphere” have dust in a spherical shell with density profile $1/r^2$ around a central point source. In those labeled “slab”, parallel rays impinge on the dusty slab. The figure shows the normalized SED ($\int f_\lambda d\lambda = 1$) of the radiation observed from outside the sphere and the non-illuminated face of the slab. The dust optical depth across the slab and along the shell radius is the same in each panel, as marked.

¹ The calculations were performed with the code DUSTY, which is publicly available at <http://www.pa.uky.edu/~moshe/dusty>

The feature behavior is affected both by the dust optical thickness and its geometry. It can be understood with the aid of the simple solution of the radiative transfer equation for the emission from dust with uniform temperature T and optical depth τ_λ :

$$I_\lambda = B_\lambda(T) \left(1 - e^{-\tau_\lambda}\right) \simeq \begin{cases} \tau_\lambda B_\lambda & \text{when } \tau_\lambda \ll 1 \\ B_\lambda & \text{when } \tau_\lambda \gg 1; \end{cases} \quad (3)$$

when the dust is exposed to external radiation with intensity I_e , the transmission term $I_e e^{-\tau_\lambda}$ is added. This result shows that the emission from optically thin dust ($\tau_\lambda \ll 1$) is proportional to the dust cross section, therefore the emergent radiation in this case follows the spectral shape shown in figure 1. A superposition of different dust temperatures preserves the proportionality with τ_λ , producing an emission feature in all optically thin sources. This feature is evident in the top panel of figure 3. The optical depth of the solutions displayed in this panel is rather small ($\tau_V = 0.15$), and the short wavelengths ($\lambda \lesssim 2\mu\text{m}$) emission is simply the input radiation, which is barely attenuated. Longer wavelengths show the dust emission, and the difference between the sphere and the slab results is an important reflection of the different temperature profiles in the two geometries. In a spherical shell, the dust temperature decreases with radial distance because of the spatial dilution of the heating radiation (eq. 1). The large range of temperatures spanned by the cool dust is reflected in the relatively broad shoulder of long-wavelength emission in the sphere solution. In contrast, the slab is exposed to parallel-rays radiation, which does not suffer any spatial dilution, therefore its temperature is uniform and the dust emission covers a more limited spectral range.

Optically thin emission increases linearly with the overall optical depth. As this optical depth approaches unity, self-absorption sets in, higher order terms in the expansion of $e^{-\tau_\lambda}$ become important and, as is evident from eq. 3, the emission saturates at the featureless Planck function: at constant temperature, emission and self-absorption exactly balance each other, producing the black-body thermodynamic limit. Therefore, a single-temperature optically thick region can never produce a feature, neither in emission nor absorption. Furthermore, irrespective of optical depth, single-temperature dust will never produce an absorption feature; it can only produce an emission feature when optically thin. The emergence of the absorption feature visible in the bottom panel of figure 3 reflects the temperature stratification in actual dusty material: as the radiation propagates from hot regions toward the observer, it passes through cooler regions where it suffers absorption that is not balanced by the emission from these cooler regions. Thus, the temperature structure primarily determines the strength of the absorption feature at large optical depths. The models displayed in this panel have $\tau_V = 150$. The input radiation is fully extinguished within a short distance from the illuminated face, creating a large

temperature gradient close to the surface. Beyond that absorption layer, the temperature profile resembles the optically thin case and is controlled by the geometry—steep decline in the spherical shell and near constancy in the slab. This difference is reflected not only in the longer wavelength emission from the spherical shell but also the much greater depth of its $10\mu\text{m}$ absorption feature.

This analysis shows that a temperature gradient is essential for an absorption feature; deep absorption requires dust geometry conducive to large gradients. Consider a cloud illuminated from outside by a radiative source. If the cloud’s dimensions are much smaller than the distance to the source, then the heating flux is constant across the cloud’s volume, just as in the slab model. Without radiative transfer effects, the dust temperature would be uniform throughout the cloud. In contrast, arranging the same dust in a geometrically thick shell around the same heating source produces a large temperature gradient because of the spatial dilution of the flux with radial distance. We can therefore expect the absorption feature to have only limited depth in the case of externally illuminated clouds. A deep feature requires the radiation source to be deeply embedded in dust that is thick both optically and geometrically. These results have important implications for the study of dust emission from active galaxies (Levenson et al., 2007; Sirocky et al., 2008).

3 Torus Phenomenology

We start with a discussion of torus observations and the physical properties that can be inferred directly from them.

3.1 IR Emission

The primary evidence for the torus comes from spectropolarimetric observations of type 2 sources, which reveal hidden type 1 emission via reflection off material situated above the torus opening. While compelling, this evidence is only indirect in that it involves obscuration, not direct emission by the torus itself. An obscuring dusty torus should reradiate in the IR the fraction of nuclear luminosity it absorbs, providing direct evidence for its existence. Indeed, the continua from most AGNs show significant IR emission. The top panel of figure 4 shows the composite type 1 spectra from a number of compilations. The optical/UV region shows the power law behavior expected from a hot disk emission. At $\lambda \gtrsim 1\mu\text{m}$, the SED shows the bump expected from dust emission. The bottom panel shows the same data after subtracting a power law fit through the short wavelengths in a crude attempt to remove the direct AGN

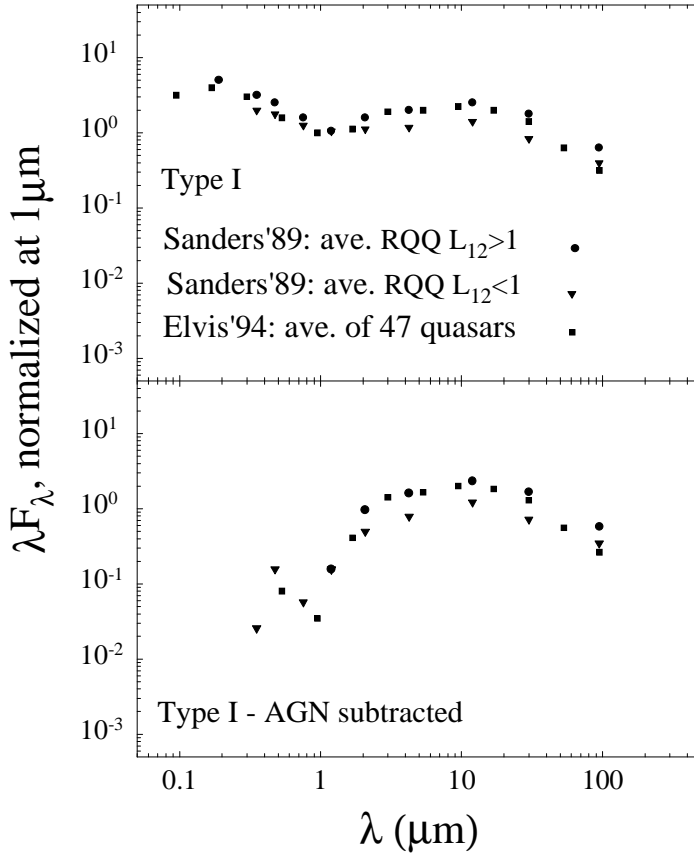


Fig. 4. SED’s of type 1 sources. Top: Average spectra from the indicated compilations; for the definition of Radio Quiet Quasars (RQQ) see Tadhunter’s lectures. Bottom: The same SED’s after subtracting a power law fit through the short wavelengths ($\lesssim 1\mu\text{m}$). These AGN-subtracted SED’s are similar to those observed in type 2 sources.

component and mimic the SED from an equatorial viewing of these sources according to the unification scheme. Indeed, the AGN-subtracted SED’s resemble the observations of type 2 sources. Silicates reveal their presence in the dust through the $10\mu\text{m}$ feature. The feature appears generally in emission in type 1 sources and in absorption in type 2 sources (Hao et al., 2007).

The torus dust emission has been resolved recently in $8\text{--}13\mu\text{m}$ interferometry with the VLTI. The first torus was detected in NGC 1068 by Jaffe et al. (2004), the second in Circinus by Tristram et al. (2007). The latter observations show evidence for the long anticipated clumpy structure. The dust temperature distributions deduced from these observations indicated close proximity between hot ($> 800\text{ K}$) and much cooler ($\sim 200\text{--}300\text{ K}$) dust. Such behavior is puzzling in the context of smooth-density calculations but is a natural consequence of clumpy models (see sec. 2.1)

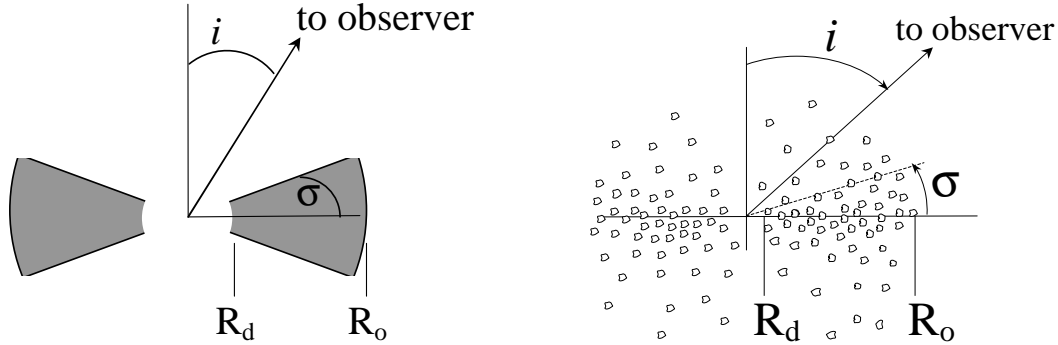


Fig. 5. AGN classification according to unified schemes. *Left:* In a smooth-density torus, the viewing angle (from the axis) $i = \frac{1}{2}\pi - \sigma$ separates between type 1 and type 2 viewing. *Right:* In a clumpy, soft-edge torus, the probability for direct viewing of the AGN decreases away from the axis, but is always finite.

3.2 Torus Obscuration

There are clear indications that the optical depth in the torus equatorial plane is at least $\tau_v \gtrsim 10$. If the dust abundance in the torus is similar to Galactic interstellar regions, the equatorial column density is at least $N_H \gtrsim 2 \times 10^{22} \text{ cm}^{-2}$.

The classification of AGN into types 1 and 2 is based on the extent to which the nuclear region is visible, therefore source statistics can determine the angular extent of the torus obscuration. In its standard formulation, the unification approach posits the viewing angle as the sole factor in determining the AGN type. This is indeed the case for a smooth-density torus that is optically thick within the angular width σ (figure 5, left sketch). All AGN viewed at $0 \leq i < \frac{1}{2}\pi - \sigma$ then appear as type 1 sources, while viewing at $\frac{1}{2}\pi - \sigma \leq i \leq \frac{1}{2}\pi$ gives type 2 appearance. If f_2 denotes the fraction of type 2 sources in the total population, then $f_2 = \sin \sigma$. This relation holds also when the column density declines smoothly with angle away from the equatorial plane. The AGN is obscured from directions that have $e^{-\tau} \gg 1$ and visible from those with $e^{-\tau} \ll 1$. Because of the steep variation of $e^{-\tau}$ with τ , the transition between these two regions is sharp, occurring around the angle where $\tau = 1$. Denoting this angle σ yields $f_2 = \sin \sigma$ irrespective of the specific angular profile. Taking account of the torus clumpiness modifies this relation fundamentally, as is evident from the right sketch in figure 5. We discuss this modification below (sec. 4.3).

From statistics of Seyfert galaxies Schmitt et al. (2001) find that $f_2 \simeq 70\%$. Employing the standard $f_2 = \sin \sigma$ relation they deduce $\sigma \simeq 45^\circ$. The issue is currently unsettled because Hao et al. (2005) have found recently that f_2 is only about 50%, or $\sigma \simeq 30^\circ$. The fraction f_2 of obscured AGN decreases with bolometric luminosity. This has been verified in a large number of observations that estimate the luminosity dependence of either f_2 or f_1 (the fraction of

unobscured sources), or differences between the luminosity functions of type 1 and 2 AGN (see Hao et al., 2005; Simpson, 2005; Maiolino et al., 2007).

3.3 *Torus Size*

Obscuration statistics provide an estimate of the torus angular width σ . Denote by H the torus height at its outer radius R_o , then $H/R_o = \tan \sigma$; obscuration does not depend individually on either H or R_o , only on their ratio. To determine an actual size one must rely on the torus emission. In the absence of high-resolution IR observations, early estimates of the torus size came from theoretical analysis of the SED. Pier & Krolik (1992) performed the first detailed calculations of dust radiative transfer in a toroidal geometry, and because of the difficulties in modeling a clumpy medium approximated the density distribution with a uniform one instead. They concluded that the torus has an outer radius $R_o \sim 5\text{--}10$ pc, but later speculated that this compact structure might be embedded in a much larger, and more diffuse, torus with $R_o \sim 30\text{--}100$ pc (Pier & Krolik, 1993). Granato & Danese (1994) extended the smooth-density calculations to more elaborate toroidal geometries. From comparisons of their model predictions with the observed IR emission at $\lambda \sim 10\text{--}25$ μm they concluded that the torus must have an outer radius $R_o \gtrsim 300\text{--}1000$ pc, and that its radial density profile must be constant; later, Granato et al. (1997) settled on hundreds of pc as their estimate for the torus size. Subsequently, $R_o \gtrsim 100$ pc became common lore.

The advent of high-resolution IR observations brought evidence in support of Pier & Krolik’s original proposal of compact torus dimensions (for details, see Nenkova et al., 2008b). It can be argued that IR observations only determine the size of the corresponding emission region and that the actual torus size could in fact be much larger, but mid-IR flux considerations were the sole reason for introducing large sizes in the first place. It seems safe to conclude that at this time there is no compelling evidence that torus clouds beyond $R_o \sim 20\text{--}30R_d$ need be considered. From eq. 2, a conservative upper bound on the torus outer radius is then $R_o < 12 L_{45}^{1/2}$ pc, where $L_{45} = L/10^{45}$ erg s $^{-1}$.

3.4 *Torus Orientation and the Host Galaxy*

Toroidal obscuration is the cornerstone of the AGN unification scheme. Since the active nucleus is at the heart of a galaxy, might the obscuration not be attributed to the host galaxy? In fact, although galactic obscuration can affect individual sources, the strong orientation-dependent absorption cannot be generally attributed to the host galaxy because the AGN axis, as traced by the jet position angle, is randomly oriented with respect to the galactic disk

in Seyfert galaxies (Kinney et al., 2000) and the nuclear dust disk in radio galaxies (Schmitt et al., 2002). In addition, Guainazzi et al. (2001) find that heavily obscured AGN reside in a galactic environment that is as likely to be ‘dust-poor’ as ‘dust-rich’.

NGC 1068, the archetype Seyfert 2 galaxy and one of the most studied active nuclei, is a revealing example. While the galaxy is oriented roughly face-on, the torus is edge-on to within $\sim 5^\circ$. The nearly edge-on orientation of the torus and accretion disk are indicated by the geometry and kinematics of both water maser (Greenhill & Gwinn, 1997; Gallimore et al., 2001) and narrow-line emission (Crenshaw & Kraemer, 2000). Some other interesting information about the AGN immediate surroundings in this source comes from molecular line observations. Schinnerer et al. (2000) find from CO velocity dispersions that at $R \simeq 70$ pc the height of the molecular cloud distribution is only $H \sim 9\text{--}10$ pc, for $H/R \sim 0.15$. Galliano et al. (2003) model the CO and H₂ emission with a clumpy molecular disk with radius 140 pc and scale height 20 pc, for the same $H/R \sim 0.15$. Thus, although resembling the putative torus, the distribution of these clouds does not meet the unification scheme requirement $H/R \sim 1$. Evidently, the detected molecular clouds are located in a thinner disk-like structure outside the torus. Galliano et al. (2003) find that this molecular disk is tilted roughly 15° from edge-on, much closer to the orientation of the AGN than of the host galaxy. Imaging polarimetry at $10\mu\text{m}$ by Packham et al. (2007) shed some light on the continuity between the torus and the host galaxy’s nuclear environments. The most recent high resolution adaptive optics observations of the nuclear region are presented by R. Davies elsewhere in these proceedings.

3.5 X-rays

AGN are strong X-ray emitters, and the X-ray observations give overwhelming evidence for the orientation-dependent absorption expected from the unification scheme. The 2–10 keV X-ray continuum from Seyfert 1 nuclei is generally unattenuated. A small amount of neutral absorption affects some of these sources, and can be attributed to the host galaxy because it is usually characterized by typical galactic column densities $N_{\text{H}} \lesssim 10^{21} \text{ cm}^{-2}$ (George et al., 1998).² In contrast, the continuum from Seyfert 2 galaxies is attenuated by obscuring columns with $N_{\text{H}} \sim 10^{22}\text{--}10^{25} \text{ cm}^{-2}$ (Bassani et al., 1999; Risaliti et al., 1999). In accordance with the unification scheme, the absorption corrected spectra and luminosities of type 2 sources are similar to those of type 1 (Smith & Done, 1996; Turner et al., 1997b). From the correla-

² Spectral features give evidence for “warm absorbers”, clouds of ionized gas with $N_{\text{H}} \sim 10^{21}\text{--}10^{23} \text{ cm}^{-2}$; see George et al for details.

tions they find among various independent absorption indicators, Bassani et al. (1999) conclude that the torus optical thickness along the line of sight is the parameter most closely correlated with the AGN X-ray properties. Prominent among these indicators is the $K\alpha$ iron line, the strongest line in the 4–10 keV X-ray spectrum of AGN. In Seyfert 1 galaxies the line equivalent width is typically ~ 150 eV (Nandra & Pounds, 1994), while in Seyfert 2 the equivalent widths are more broadly distributed, ranging from about 100 eV to 1 keV (Turner et al., 1997a) and even 5 keV in some Compton-thick AGN (Levenson et al., 2002). The Seyfert 2 equivalent widths reflect processing in a toroidal structure around the nucleus (Krolik et al., 1994; Levenson et al., 2002).

Yet in spite of the overall correspondence between the optical and X-ray obscuration, there is a significant number of AGN for which the expected characteristics are different in the two bands. Although substantial X-ray absorption is common among type 2 AGN, there are also unabsorbed X-ray sources that present only narrow emission lines in their optical spectra. Such cases can be explained with the observational selection effect suggested by Severgnini et al. (2003) and Silverman et al. (2005): in these sources, the optical light of the host galaxy outshines the AGN continuum and broad lines. This suggestion was supported by the subsequent studies of Page et al. (2006) and Garcet et al. (2007). In addition, some of the low-luminosity cases may reflect the disappearance of both torus obscuration and broad line emission (see sec. 5.3 below). The opposite case, obscuration only in X-rays, exists too—there are type 1, broad line AGN with significant X-ray absorption (Perola et al., 2004; Eckart et al., 2006; Garcet et al., 2007). Extreme cases include quasars whose optical spectrum shows little or no dust extinction while their X-ray continuum is heavily affected by Compton thick absorption (Braitto et al., 2004; Gallagher et al., 2006). This cannot be attributed to observational selection effects.

The differences observed in some sources between X-ray and UV/optical attenuation arise naturally from the different absorption properties of gas and dust. Dusty material absorbs continuum radiation both in the UV/optical and X-rays, therefore the dusty torus provides obscuration of both. But dust-free gas attenuates just the X-ray continuum, so clouds inside the dust sublimation radius will provide obscuration only in this band. Conclusive evidence for such obscuration comes from the short time scales for transit of X-ray absorbing clouds across the line of sight, which establish the existence of obscuring clouds inside the dust sublimation radius (Risaliti et al., 2002). Extreme cases involve 4 hour variability (Elvis et al., 2004) and variations in absorbing column of more than 10^{24} cm^{-2} within two days, indicating Compton thick ($N_{\text{H}} > 10^{24} \text{cm}^{-2}$) X-ray absorption from a single cloud in the broad-lines region (Risaliti et al., 2007). These observations show that the torus extends inward beyond the dust sublimation point to some inner radius $R_{\text{x}} < R_{\text{d}}$.

Clouds at $R_x \leq r \leq R_d$ partake in X-ray absorption but do not contribute appreciably to optical obscuration or IR emission because they are dust-free. Since every cloud that attenuates the optical continuum contributes also to X-ray obscuration but not the other way round, the X-ray absorbing column should be at least as large as the UV/optical absorbing column, as observed (Maccacaro et al., 1982). Further, Maiolino et al. (2001) find that the X-ray absorbing column exceeds the reddening column in each member of an AGN sample by a factor ranging from ~ 3 up to ~ 100 . Although this discrepancy could also arise from unusual dust-to-gas ratio or dust properties, the observational evidence for X-ray absorption by clouds in the dust-free inner portion of the torus implies that in all likelihood, these clouds provide the bulk of the absorption. This could explain the Guainazzi et al. (2005) finding that at least 50% of Seyfert 2 galaxies are Compton thick.

3.6 X-ray vs IR

IR flux measurements collect the emission from the entire torus area on the plane of the sky, originating from clouds along all rays through the torus. In contrast, X-ray attenuation is controlled by the clouds along just one particular ray, the line of sight to the AGN. Therefore, even for the dusty portion of the obscuring column, the number of X-ray absorbing clouds can differ substantially from the torus average. Two type 2 sources with similar cloud properties and the same overall number of clouds following the same spatial distribution will have an identical IR appearance, yet their X-ray absorbing columns could still differ significantly. This can be expected to introduce a large scatter in torus X-ray properties among AGN with similar IR emission. It may help explain why the SEDs show only moderate variations in the infrared that are not well correlated with the X-ray absorbing columns (e.g., Silva et al., 2004).

4 Clumpiness—Handling and Implications

The clumpy nature of the environment around the central black-hole is crucial for understanding various aspects of AGN observations. We start by presenting a general formalism developed in Nenkova et al. (2002, 2008a) for handling clumpy media. The original development, described here, applies only to continuum emission and takes all clouds to be identical, for simplicity. The formalism was extended to line emission and to a mixture of cloud properties by Conway, Elitzur, & Parra (2005, 2008).

4.1 Clumpy Radiative Transfer

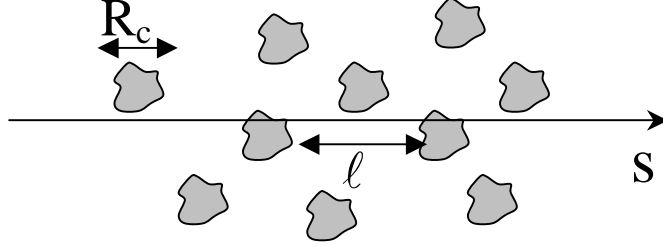


Fig. 6. A region populated by clouds of size R_c . Along ray s , the photon mean-free-path is ℓ and the number of clouds per unit length is $N_C = \ell^{-1}$.

Figure 6 sketches a region where the matter is concentrated in clouds. Individual clouds are characterized by their size R_c , the cloud distribution is specified by the number of clouds per unit volume n_C . It is useful to introduce the number of clouds per unit length $N_C = n_C A_c = \ell^{-1}$ where A_c is the cloud cross-sectional area and ℓ is the photon mean free path for travel between clouds. Denote by V_c the volume of a single cloud and by ϕ the volume filling factor of all clouds, i.e., the fraction of the overall volume that they occupy. The medium is clumpy whenever

$$\phi = n_C V_c \ll 1. \quad (4)$$

In contrast, the matter distribution is smooth, or continuous, when $\phi \simeq 1$. Since $V_c \simeq A_c R_c$, the clumpiness condition is equivalent to

$$\phi = N_C R_c \ll 1, \quad \text{or} \quad R_c \ll \ell. \quad (5)$$

The clumpiness criterion is met when the mean free path between clouds greatly exceeds the cloud size. Under these circumstances, each cloud can be considered a “mega-particle”, a point source of intensity $S_{c,\lambda}$ and optical depth τ_λ . The intensity at an arbitrary point s along a given path can then be calculated by applying the formal solution of radiative transfer to the clumpy medium. The intensity generated in segment ds' around a previous point s' along the path is $S_{c,\lambda}(s')N_C(s')ds'$. Denote by $\mathcal{N}(s', s) = \int_{s'}^s N_C ds$ the mean number of clouds between s' and s and by $P_{\text{esc}}(s', s)$ the probability that the radiation from s' will reach s without absorption by intervening clouds. The number distribution of clouds between s' and s follows Poisson statistics around the mean $\mathcal{N}(s', s)$, and Natta & Panagia (1984) show that

$$P_{\text{esc}}(s', s) = e^{-t_\lambda(s', s)}, \quad \text{where} \quad t_\lambda(s', s) = \mathcal{N}(s', s)(1 - e^{-\tau_\lambda}). \quad (6)$$

The intuitive meaning of this result is straightforward in two limiting cases. When $\tau_\lambda < 1$ we have $t_\lambda(s', s) \simeq \mathcal{N}(s', s)\tau_\lambda$, which is the overall optical depth between points s' and s ; that is, clumpiness is irrelevant when individual clouds are optically thin, and the region can be handled with the smooth-density approach. It is important to note that $\mathcal{N}\tau_\lambda$ can be large—the only requirement for this limit is that each cloud be optically thin. The opposite limit $\tau_\lambda > 1$ gives $P_{\text{esc}}(s', s) \simeq e^{-\mathcal{N}(s', s)}$. Even though each cloud is optically thick, a photon can still travel between two points along the path if it avoids all the clouds in between. With this result, the intensity at s generated by clouds along the given ray is

$$I_\lambda^{\text{C}}(s) = \int_0^s e^{-t_\lambda(s', s)} S_{\text{c},\lambda}(s') N_{\text{C}}(s') ds' \quad (7)$$

This relation is the exact analog of the formal solution of standard radiative transfer in continuous media, to which it reverts when the cloud sizes are decreased to the point that they become microscopic particles; in that case $\tau \ll 1$ for each particle and ℓ^{-1} is the standard absorption coefficient. The result does not involve ϕ ; only N_{C} enters. A complete formalism that would not invoke the assumption $\phi \ll 1$ would lead to a series expansion in powers of ϕ , and our derived expression would yield the zeroth order term in that expansion. In fact, detailed Monte Carlo simulations show that, to within a few percents, our result describes adequately clumpy media with ϕ as large as 10%, as shown in figure 7. Since the intensity calculations are independent of the volume filling factor, modeling results do not provide any information on this quantity, nor do they provide separate information on either R_{c} or n_{C} , only on N_{C} . In complete analogy, the radiative transfer problem for smooth density distributions does not involve separately the size of the dust grains or their volume density, only the combination $n_{\text{d}}\sigma_{\text{d}}$, which determines the absorption coefficient and which is equivalent to N_{C} .

An intensity calculation requires the cloud source function $S_{\text{c},\lambda}$ at every location in the clump distribution (eq. 7). Since the clump emission is anisotropic, as is evident from figure 2, $S_{\text{c},\lambda}$ depends not only on location but also on the observer's position angle α . It is convenient to split the population of clumps to those that are directly exposed to the AGN radiation, with a source function $S_{\text{c},\lambda}^{\text{d}}$, and those shadowed by intervening clouds. The latter are heated only indirectly by the emission from all other clouds and their source function is denoted $S_{\text{c},\lambda}^{\text{i}}$. At location (r, β) , where β is angle from the equatorial plane, the mean number of clouds to the AGN is $\mathcal{N}(r, \beta) = \int_0^r N_{\text{C}}(r, \beta) dr$ and the probability for unhindered view of the AGN is $p(r, \beta) = e^{-\mathcal{N}(r, \beta)}$. The general expression for the cloud overall source function is thus

$$S_{\text{c},\lambda}(r, \alpha, \beta) = p(r, \beta) S_{\text{c},\lambda}^{\text{d}}(r, \alpha) + [1 - p(r, \beta)] S_{\text{c},\lambda}^{\text{i}}(r, \alpha, \beta) \quad (8)$$

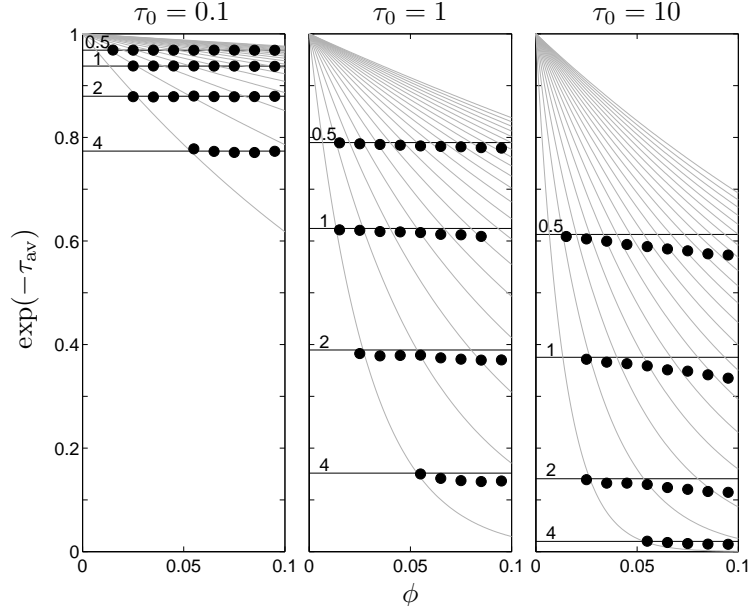


Fig. 7. Averaged transmission, $\exp(-\tau_{\text{av}})$, through a clumpy region with filling factor ϕ . The optical depth of a single cloud is τ_0 , as marked on top each panel; all $\tau_0 \geq 10$ are equivalent. Horizontal lines show the theoretical small- ϕ limit (eq. 6); they are labeled by the mean number of clouds along a line through the volume. The results of Monte Carlo simulations are shown with filled circles whose sizes are comparable to the numerics error bars. Gray curves trace the loci of constant cloud sizes. The analytical expression adequately describes clumpy regions with ϕ as large as 10% (Conway et al., 2008).

The source functions $S_{c,\lambda}^{\text{d}}$ can be calculated from a straightforward solution of the standard radiative transfer problem once a geometrical shape is assumed for the individual clouds, a calculation that is independent of the cloud distribution. The indirect heating of shadowed clouds, on the other hand, involves the radiation from all other clouds and thus cannot be calculated without solving the full problem. This is the difficulty presented by diffuse radiation in standard radiative transfer. Since the diffuse heating is dominated by the clouds that are directly heated by the AGN, the $S_{c,\lambda}^{\text{d}}$ source functions can serve as the starting point for an iterative solution of the full problem: From the emission of the directly heated clouds devise a first approximation for the diffuse radiation field. Next, place clouds in this radiation field and calculate their emission to derive a first approximation for the source functions of indirectly illuminated clouds and, from eq. 8, the composite source function at every location. In successive iterations, add to the AGN direct field the cloud radiation calculated from eq. 7, and repeat the process until convergence. Nenkova et al. (2002, 2008a) performed only the first step of this procedure, an approximation that leaves out the feedback effect of the clouds on their own radiative heating. Carrying out higher orders of the iteration scheme is an open challenge.

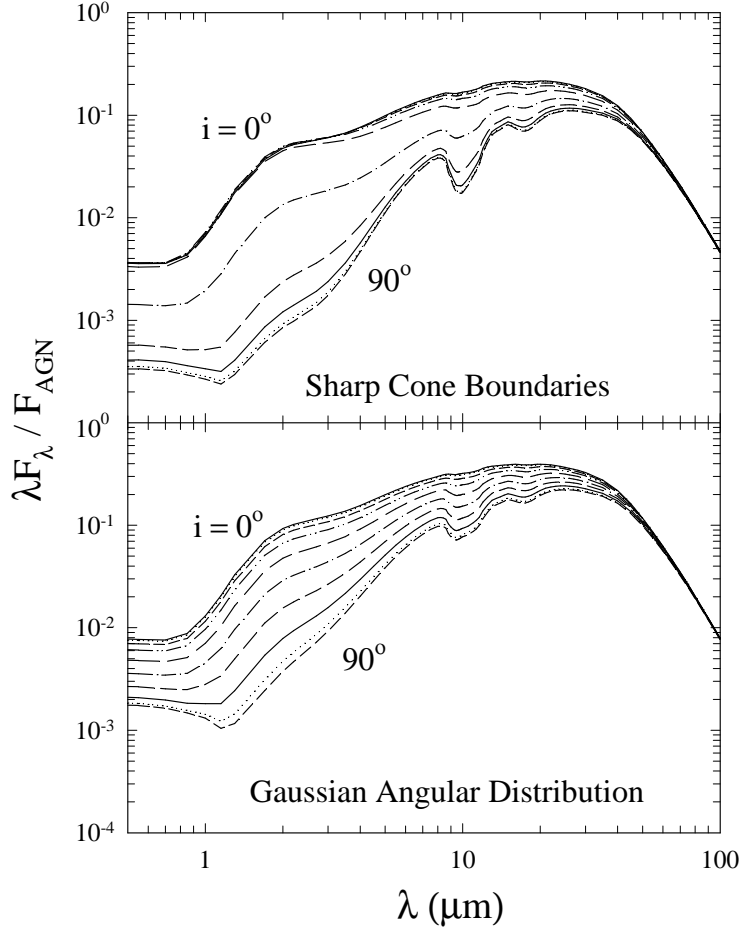


Fig. 8. Model spectra for dust IR radiation of a clumpy torus. In the bottom panel the cloud distribution follows eq. 9 with $\mathcal{N}_0 = 5$, $\sigma = 45^\circ$ and $q = 1$ in the radial range $R_d \leq r \leq 30R_d$. Each cloud has an optical depth $\tau_V = 60$. Models in the top panel are the same, except that the angular distribution is uniform within $|\beta| \leq \sigma$. Different curves show viewing angles that vary in 10° steps from pole-on ($i = 0^\circ$) to edge-on ($i = 90^\circ$). Fluxes are scaled with $F_{\text{AGN}} = L/4\pi D^2$. (Nenkova et al., 2008b)

4.2 Clumpy Torus Emission

The only distribution required for calculating the intensity from eq. 7 is N_C , the number of clouds per unit length. The torus axial symmetry implies that N_C depends only on the distance r from the center and the angle β from the equatorial plane (the complementary of the standard polar angle). Denote by \mathcal{N}_0 the mean of the total number of clouds along radial rays in the equatorial plane. We parametrize the angular profile of the cloud distribution as a Gaussian with width parameter σ and the radial distribution as a declining power law with index q , so that

$$N_C(r, \beta) = \frac{C}{R_d} \mathcal{N}_0 e^{-\beta^2/\sigma^2} \left(\frac{R_d}{r}\right)^q \quad (9)$$

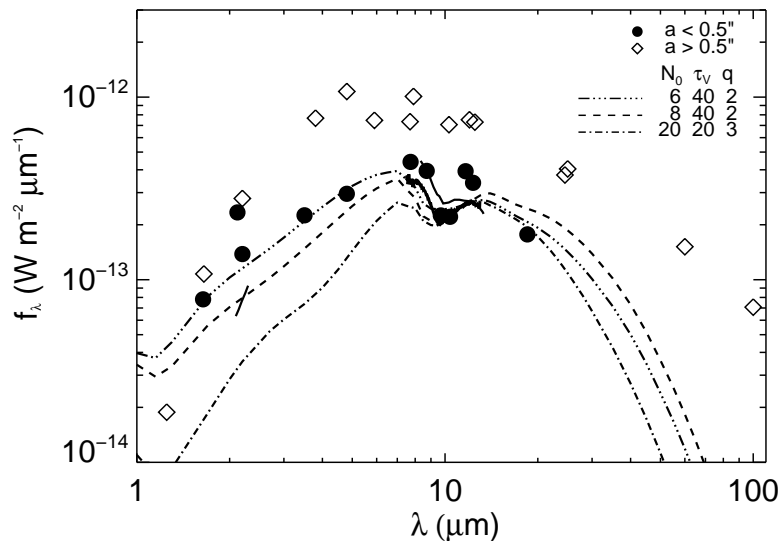


Fig. 9. Fits of clumpy torus models to small-aperture ($0.4''$) Gemini 8–13 μm spectrum of NGC 1068, shown with heavy solid line. Symbols and thin solid line between 8–13 μm mark all other data, which were not utilized in the fits. Filled symbols denote measurements with aperture $a < 0.5''$, open symbols $a > 0.5''$. Model spectra are for equatorial viewing and various parameters (for details see Mason et al., 2006).

where $C = (\int_1^Y dy/y^q)^{-1}$ is a dimensionless constant, ensuring the normalization $\mathcal{N}_0 = \int N_C(r, \beta = 0) dr$. The Gaussian can be taken as representative of soft-edge angular distributions, illustrated on the right in figure 5. Sharp-edge angular distributions can be parametrized with a step function with cutoff at $\beta = \sigma$. Figure 8 shows the results of model calculations for these two geometries with the same set of parameters. The sharp-edge geometry produces a bimodal distribution of spectral shapes, with little dependence on viewing angle other than the abrupt change that occurs between the torus opening and the obscured region. This SED dichotomy conflicts with observations (Alonso-Herrero et al., 2003). In contrast, the soft-edge Gaussian distribution produces a larger variety in model spectral shapes, with a smooth, continuous dependence on i , in agreement with the findings of Alonso-Herrero et al. (2003). It is gratifying that the more plausible soft-edge distribution also produces better agreement with observations.

Clumpy torus modeling was employed in the analysis of spatially-resolved, near-diffraction-limited 10 μm spectra of the nucleus of NGC 1068, obtained by Mason et al. (2006) with Michelle, the mid-IR imager and spectrometer on the Gemini North telescope. Mason et al first compared the models with the 8–13 μm Michelle spectrum of the central $0.4''$ core to determine the best-fit parameters. The model predictions outside this spectral range were then compared with all other observations, and figure 9 shows the results of this

comparison. As noted above, the torus in this AGN is nearly edge-on (sec. 3.4), and this is the first model to reproduce the observed near-IR flux with such orientation; in contrast, smooth-density models were forced to assume, contrary to observations, viewing from 22° – 25° above the equatorial plane in order to bring into view the warm face of the torus backside (Granato et al., 1997; Gratadour et al., 2003; Fritz et al., 2006). It is noteworthy that all flux measurements with apertures $< 0.5''$ are in good agreement with the model results. However, the flux collected with larger apertures greatly exceeds the model predictions at wavelengths longer than $\sim 4\mu\text{m}$. This discrepancy can be attributed to IR emission from nearby dust outside the torus—Mason et al show that the torus contributes less than 30% of the $10\mu\text{m}$ flux collected with apertures $\geq 1''$. The bulk of the large-aperture flux comes at these wavelengths from dust in the ionization cones³; while less bright than the torus dust, it occupies a much larger volume. On the other hand, the torus dominates the emission at short wavelengths; at $2\mu\text{m}$, more than 80% of the flux measured with apertures $\geq 1''$ comes from the torus even though its image size is less than $0.04''$ (Weigelt et al., 2004). This highlights a difficult problem that afflicts all IR studies of AGN. The torus emission can be expected to dominate the observed flux at near IR because such emission requires hot dust that exists only close to the center. But longer wavelengths originate from cooler dust, and the torus contribution can be overwhelmed by the surrounding regions. There are no easy solutions to this problem.

All in all, clumpy torus models seem to produce SED's that are in reasonable overall agreement with observations for the following range of parameters (Nenkova et al., 2002, 2008a,b):

- Number of clouds, on average, along radial equatorial rays $\mathcal{N}_0 = 5$ – 15
- Gaussian angular distribution with width $\sigma = 30^\circ$ – 50°
- Index of power law radial distribution $q = 1$ – 2
- Optical depth, at visual, of each cloud $\tau_V = 30$ – 100
- The torus extends from dust sublimation at $R_d = 0.4L_{45}^{1/2}$ pc to an outer radius $R_o > 5R_d$

The silicate features display in clumpy models a complex behavior that cannot be reproduced with smooth-density distributions. Figure 10 shows some model results for the spectral region containing the features. The depth of the absorption features is never large in spite of the huge optical depths of some of the displayed models—a torus with $\tau_V = 150$ and $\mathcal{N}_0 = 10$ has an equatorial optical depth of 1500 at visual. The relatively shallow absorption reflects the small temperature gradient across an externally illuminated cloud, similar to the slab case (see sec. 2.2, fig. 3). Indeed, a striking characteristic of all AGN spectra is the absence of any deep $10\mu\text{m}$ absorption features in

³ For discussion of ionization cones see lectures by Netzer, Peterson and Tadhunter.

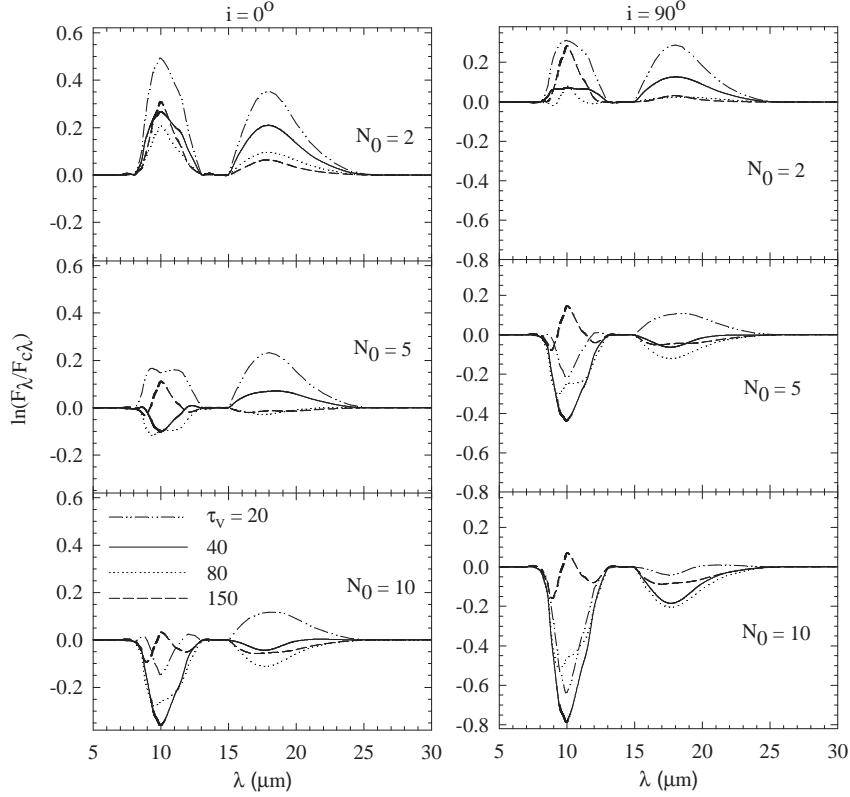


Fig. 10. Spectral shape of the silicate 10 and 18 μm features: F_λ is the torus emission in the 5–30 μm region and $F_{c,\lambda}$ is the smooth underlying continuum obtained by a spline connecting the feature-free segments in this spectral region. All models have $q = 2$, $R_o = 30R_d$, $\sigma = 45^\circ$, and \mathcal{N}_0 as marked in each panel. Curves correspond to different τ_V , as labeled. Panels on the left correspond to pole-on viewing, on the right to edge-on; note the different scales of the vertical axes in the two cases. (Nenkova et al., 2008b)

contrast with Ultraluminous IR Galaxies (ULIRGs) where the features reach extreme depths (Hao et al., 2007). This different behavior in ULIRGs can be attributed to deep embedding in a dust distribution that is smooth, rather than clumpy (Levenson et al. 2007; see also Spoon et al. 2007, Sirocky et al. 2008). A most peculiar result is the emergence of the 10 μm feature in *emission* at equatorial viewing when τ_V is large for all \mathcal{N}_0 , and when \mathcal{N}_0 is small for all τ_V . This could explain intriguing *Spitzer* observations of seven high-luminosity type 2 QSOs by Sturm et al. (2006). Although the individual spectra appear featureless, the sample average spectrum shows the 10 mic feature in emission. Therefore, if this finding is verified it could indicate that the optical depths of torus clouds perhaps are larger in QSOs than in Seyfert galaxies or that the cloud number \mathcal{N}_0 decreases as the luminosity increases.

While the parameters listed above lead to SED's compatible with observations, some additional considerations can further restrict the acceptable range. For example, in spite of the huge difference in AGN obscuration between type

1 and 2 sources, comparisons of their IR emission seem to indicate a surprisingly low amount of anisotropy (Lutz et al., 2004; Buchanan et al., 2006; Horst et al., 2006). Models with $q = 2$ tend to produce less variation with viewing-angle than those with $q = 1$. Therefore, observations that will place reliable tight constraints on the IR emission anisotropy may indicate that $q = 2$ provides a more appropriate description of the radial distribution than $q = 1$. Finally, all model calculations were performed with standard Galactic ISM dust, which seems to provide satisfactory results. Current data do not provide any compelling reason for drastic changes in the dust composition.

4.3 Clumpy Unification

Because of clumpiness, the difference between types 1 and 2 is not truly an issue of orientation but of probability for direct view of the AGN (figure 5, right sketch); *AGN type is a viewing-dependent probability*. Since that probability is always finite, type 1 sources can be detected from what are typically considered type 2 orientations, even through the torus equatorial plane: if $\mathcal{N}_0 = 5$, for example, the probability for that is $e^{-5} = 1/148$ on average. This might offer an explanation for the few Seyfert galaxies reported by Alonso-Herrero et al. (2003) to show type 1 optical line spectra together with 0.4–16 μm SED that resemble type 2. Conversely, if a cloud happens to obscure the AGN from an observer, that object would be classified as type 2 irrespective of the viewing angle. In cases of such single cloud obscuration, on occasion the cloud may move out of the line-of-sight, creating a clear path to the nucleus and a transition to type 1 spectrum. Such transitions between type 1 and type 2 line spectra have been observed in a few sources (see Aretxaga et al., 1999, and references therein). It is worth while to conduct monitoring observations in an attempt to detect additional such transitions. The most promising candidates would be obscured systems with relatively small X-ray obscuring columns, small torus sizes (low AGN luminosity; see eq. 2) and large black-hole masses (Nenkova et al., 2008b).

A sharp-edge clumpy torus has $f_2 = (1 - e^{-\mathcal{N}_0}) \sin \sigma$, which is practically indistinguishable from the smooth-density relation when \mathcal{N}_0 exceeds ~ 3 –4 (see sec. 3.2). However, the situation changes fundamentally for soft-edge clumpy distributions because at every viewing angle, the probability of obscuration increases with the number of clouds. As is evident from figure 11, the Gaussian distribution produces a strong dependence on \mathcal{N}_0 and significant differences from the sharp-edge case. Since the sharp-edge angular distribution is ruled out by observations, *the fraction of obscured sources depends not only on the torus angular width but also on the average number of clouds along radial rays*. While the fraction $f_2 = 70\%$ requires $\sigma = 45^\circ$ in the smooth-density case, it implies $\sigma = 33^\circ$ in a Gaussian clumpy torus with $\mathcal{N}_0 = 5$ clouds.

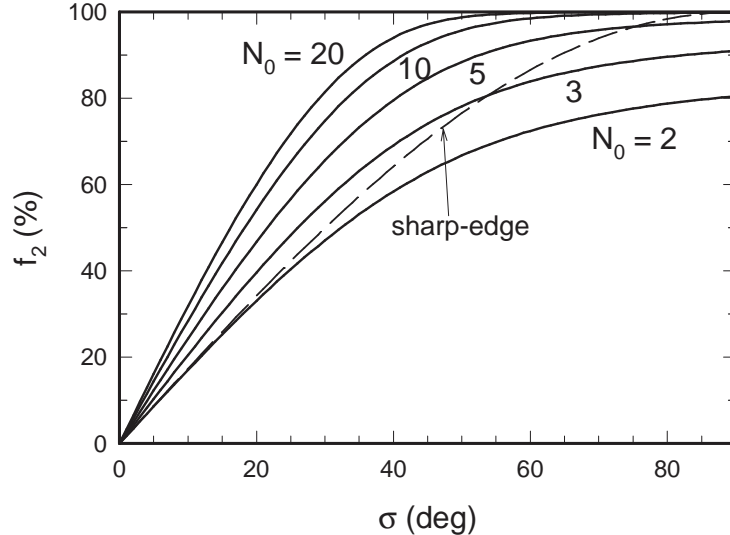


Fig. 11. AGN statistics: The fraction f_2 of obscured sources as a function of the torus width parameter σ . In torii with either smooth density distribution or a sharp-edge clumpy one, this fraction is determined uniquely by σ , and is shown with the dashed line. In contrast, in a clumpy torus with Gaussian angular distribution (eq. 9), f_2 depends on both σ and the cloud number \mathcal{N}_0 , which is marked on the various solid lines (Nenkova et al., 2008b).

Observations show that f_2 decreases with L . This has been interpreted as support for the “receding torus” model, in which σ decreases with L (Simpson 2005 and references therein). However, all the quantitative analyses performed thus far for the L -dependence of f_2 were based on the sharp-edge expression $f_2 = \sin \sigma$. Removing this assumption affects profoundly the foundation of the receding torus model because the dependence on the number of clouds necessitates analysis with two free parameters, therefore σ cannot be determined without \mathcal{N}_0 . A decrease of \mathcal{N}_0 with L at constant σ will also produce a decrease in f_2 , the same effect as a decrease of σ (figure 11). An observed trend of f_2 with L may arise from a dependence on either σ or \mathcal{N}_0 or both. There is no obvious a-priori means for deciding between the various possibilities.

4.4 Torus Mass; Total Number of Clouds

The total mass in torus clouds can be written as $M_{\text{torus}} = m_p N_H \int N_C(r, \beta) dV$, where m_p is the proton mass and N_H is the column density of a single cloud; note that M_{torus} does not involve the volume filling factor. Denote $Y = R_o/R_d$ the torus radial thickness. With the cloud distribution from eq. 9 and taking for simplicity a sharp-edge angular distribution, so that the integration is analytic, the torus mass is $M_{\text{torus}} = 4\pi m_p \sin \sigma N_{\text{torus}} R_d^2 Y I_q(Y)$, where $I_q = 1$, $Y/(2 \ln Y)$ and $\frac{1}{3}Y$ for $q = 2$, 1 and 0, respectively. Taking R_d from eq. 2,

the mass ratio of the torus and the central black hole is

$$\frac{M_{\text{torus}}}{M_{\bullet}} = 2 \times 10^{-4} \frac{L}{L_{\text{Edd}}} \sin \sigma N_{\text{torus},23} Y I_q \quad (10)$$

where L_{Edd} is the Eddington luminosity and $N_{\text{torus},23}$ is the equatorial column density in 10^{23} cm^{-2} . Since the Eddington ratio L/L_{Edd} is always < 1 and the radial thickness Y is in all likelihood no larger than $\sim 20\text{--}30$ (sec. 3.3), the torus mass is always negligible in comparison with M_{\bullet} when $q = 2$. If the radial cloud distribution is flatter, eq. 10 may constrain the torus properties to keep its mass below that of the black-hole.

The total number of torus clouds is $n_{\text{tot}} = \int n_C dV = \int (N_C/A_c) dV$. This is the only quantity of interest that depends explicitly on the cloud size. Equivalently, R_c can be replaced by the volume filling factor ϕ , since inserting eq. 9 into eq. 5 yields $R_c = C\phi R_d/\mathcal{N}_0$ at the torus inner edge. If ϕ is constant throughout the torus then $n_{\text{tot}} \simeq \mathcal{N}_0^3/\phi^2$ for the $1/r^2$ distribution, independent of the torus radial thickness Y . For example, if the volume filling factor is 10%, in order to encounter $\mathcal{N}_0 = 5\text{--}10$ clouds along each radial equatorial ray, the torus must contain $n_{\text{tot}} \simeq 10^4\text{--}10^5$ clouds,

5 What is the Torus?

In the ubiquitous sketch by Urry & Padovani (1995), shown numerous times also in this summer school, the AGN central region, comprised of the super-massive black hole (SBH), its accretion disk and the broad-line emitting clouds, is surrounded by a large doughnut-like structure—the torus. This hydrostatic object is a separate entity, presumably populated by molecular clouds accreted from the galaxy. Gravity controls the orbital motions of the clouds, but the origin of vertical motions capable of sustaining the “doughnut” as a hydrostatic structure whose height is comparable to its radius was recognized as a problem since the first theoretical study by Krolik & Begelman (1988). An entirely different scenario, hydrodynamic rather than hydrostatic, was proposed by Emmering et al. (1992). It involves the outflow of clouds embedded in a hydromagnetic disk wind, avoiding the vertical support problem. The clouds are accelerated by the system rotation along magnetic field lines anchored in the disk in a manner first described in the Blandford & Payne (1982) seminal work. In this approach the torus is merely a region in the wind which happens to provide the required toroidal obscuration because the clouds there are dusty and optically thick. That is, instead of a hydrostatic “doughnut”, the torus is just one region in a clumpy wind coming off the black-hole accretion disk. The wind paradigm was strongly advocated by A. Königl and his associates (Königl & Kartje, 1994; Kartje & Königl, 1996; Kartje et al., 1999; Everett,

2005) and by Bottorff et al. (1997, 2000) but did not gain wide acceptance until recently because of the general perception that the torus must extend to more than ~ 100 pc, a distance too large to support the required disk wind.

Recent observations suggest that the disk wind scenario might offer the better paradigm for the AGN torus (Elitzur & Shlosman, 2006). High-resolution IR observations indicate that the torus size might actually be no more than a few pc (sec. 3.3). This compact size places the torus clouds well inside the black hole sphere of influence, where the SBH gravity dominates over the galactic bulge. The outer boundary of this region is where the SBH and the bulge induce gravitational rotations with equal angular velocities, i.e., the radius within which the bulge mass is equal to that of the black hole. Consider a spherical bulge that induces a linearly rising rotation curve with $\Omega \sim 1 \text{ km s}^{-1} \text{ pc}^{-1}$, as is typical of AGN host galaxies (Sofue et al., 1999), and an SBH with a mass of $M_{\bullet,7} \times 10^7 M_{\odot}$ at its center. The SBH will dominate the gravitational motions within a radius $35 \text{ pc} \times (M_{\bullet,7}/\Omega_1^2)^{1/3}$, where $\Omega_1 = \Omega/(1 \text{ km s}^{-1} \text{ pc}^{-1})$. Since the torus is well within this sphere of influence, its dynamic origin is determined in all likelihood not by the host galaxy but by the central engine and its accretion disk. There is mounting evidence for cloud outflow in these regions with the geometry and kinematics of disk winds (e.g., Elvis, 2004; Gallagher & Everett, 2007), in accord with the outflow paradigm.

Two different types of observations show that the torus is a smooth continuation of the broad lines region (BLR), not a separate entity. IR reverberation observations by Suganuma et al. (2006) measure the time lag of the dust radiative response to temporal variations of the AGN luminosity, determining the torus innermost radius. Their results show that this radius scales with luminosity as $L^{1/2}$ and is uncorrelated with the black hole mass, demonstrating that the torus inner boundary is controlled by dust sublimation (eq. 2), not by dynamical processes. Moreover, in each AGN for which both data exist, the IR time lag is the upper bound on all time lags measured in the broad lines, a relation verified over a range of 10^6 in luminosity. This finding shows that the BLR extends outward all the way to the inner boundary of the dusty torus, validating the Netzer & Laor (1993) proposal that the BLR size is bounded by dust sublimation. The other evidence is the finding by Risaliti et al. (2002) that the X-ray absorbing columns in Seyfert 2 galaxies display time variations caused by cloud transit across the line of sight. Most variations come from clouds that are dust free because of their proximity (< 0.1 pc) to the AGN, but some involve dusty clouds at a few pc. Other than the different time scales for variability, there is no discernible difference between the dust-free and dusty X-ray absorbing clouds, nor are there any gaps in the distribution. These observations show that the X-ray absorption, broad line emission and dust obscuration and reprocessing are produced by a single, continuous distribution of clouds. The different radiative signatures merely reflect the change in cloud composition across the dust sublimation radius R_d . The inner clouds are

dust free. Their gas is directly exposed to the AGN ionizing continuum, therefore it is atomic and ionized, producing the broad emission lines. The outer clouds are dusty, therefore their gas is shielded from the ionizing radiation, and the atomic line emission is quenched. Instead, these clouds are molecular and dusty, obscuring the optical/UV emission from the inner regions and emitting IR. Thus the BLR occupies $r < R_d$ while the torus is simply the $r > R_d$ region. Both regions absorb X-rays, but because most of the clouds along each radial ray reside in its BLR segment, that is where the bulk of the X-ray obscuration is produced. Since the unification torus is just the outer portion of the cloud distribution and not an independent structure, it is appropriate to rename it the TOR for Toroidal Obscuration Region. The close proximity of BLR and TOR clouds should result in cases of partial obscuration, possibly leading to observational constraints on cloud sizes.

The merger of the ionized and the dusty clouds into a single population fits naturally into the TOR outflow paradigm. The AGN accretion disk appears to be fed by a midplane influx of cold, clumpy material from the main body of the galaxy (Shlosman et al., 1990, and references therein). Approaching the center, conditions for developing hydromagnetically- or radiatively-driven winds above this equatorial inflow become more favorable. The disk-wind rotating geometry provides a natural channel for angular momentum outflow from the disk (Blandford & Payne, 1982) and is found on many spatial scales, from protostars to AGN. The composition along each streamline reflects the origin of the outflow material at the disk surface. The disk outer regions are dusty and molecular, as observed in water masers in some edge-on cases (Greenhill, 2005), and clouds uplifted from these outer regions feed the TOR. Such clouds have been detected in water maser observations of Circinus (Greenhill et al., 2003) and NGC 3079 (Kondratko et al., 2005). The Circinus Seyfert 2 core provides the best glimpse of the AGN dusty/molecular component. Water masers trace both a Keplerian disk and a disk outflow (Greenhill et al., 2003). Dust emission at 8–13 μ m shows a disk embedded in a slightly cooler and larger, geometrically thick torus (Tristram et al., 2007). The dusty disk coincides with the maser disk in both orientation and size. The outflow masers trace only parts of the torus. The lack of full coverage can be attributed to the selectivity of maser operation—strong emission requires both pump action to invert the maser molecules in individual clouds and coincidence along the line of sight in both position and velocity of two maser clouds (Kartje et al., 1999). In NGC 3079, four maser features were found significantly out of the plane of the maser-traced disk yet their line-of-sight velocities reflect the velocity of the most proximate side of the disk. Kondratko et al. (2005) note that this can be explained if, as proposed by Kartje et al. (1999), maser clouds rise to high latitudes above the rotating structure while still maintaining, to some degree, the rotational velocity imprinted by the parent disk. Because the detected maser emission involves cloud-cloud amplification that requires precise alignment in both position and velocity along the line-of-sight, the

discovery of four high-latitude maser features implies the existence of many more such clouds partaking in the outflow in this source. Moving inward from the dusty/molecular regions, at some smaller radius the dust is destroyed and the disk composition switches to atomic and ionized, producing a double-peak signature in some emission line profiles (Eracleous, 2004). The outflow from the atomic/ionized inner region feeds the BLR and produces many atomic line signatures, including evidence for the disk wind geometry (Hall et al., 2003).

The outflow paradigm for the obscuring torus provides what can be called a “Grand Unification Theory” for AGN. This picture requires only the accretion disk and the clumpy outflow it generates—there is no need to invoke any additional, separate structure such as a hydrostatic “doughnut”. Cloud radial distance from the AGN center and vertical height above the accretion disk explain the rich variety of observed radiative phenomena. In both the inner and outer outflow regions, as the clouds rise and move away from the disk they expand and lose their column density, limiting the vertical scope of X-ray absorption, broad line emission and dust obscuration and emission. The result is a toroidal geometry for both the BLR and the TOR. With further rise and expansion, the density decreases so the ionization parameter increases, turning the clouds into members of the warm absorber population (see lectures by H. Netzer elsewhere in these proceedings). Similar considerations can be invoked to explain the broad absorption lines observed in some quasars (BAL/QSO; Gallagher & Everett, 2007). We proceed now to discuss some consequences of the TOR outflow scenario.

5.1 TOR Cloud Properties

The only property of individual clouds constrained from the IR modeling is their optical depth. It should lie in the range $\tau_V \sim 30\text{--}100$ (sec. 4.2), i.e., the cloud column density is $N_H \sim 10^{22}\text{--}10^{23} \text{ cm}^{-2}$ assuming standard dust-to-gas ratio. Clouds uplifted into the wind expand while moving away from the disk and their column density decreases. A cloud starting with $N_H \sim 10^{23} \text{ cm}^{-2}$ ceases to partake in obscuration when its column is reduced by ~ 100 so that its τ_V drops below unity. Clouds starting with a smaller column will rise to a smaller height before losing their obscuration and leaving the TOR population. The obscuration properties constrain only the cloud column density, the product of the cloud’s size and density. The latter can be constrained separately when we note that the cloud must be able to withstand the black-hole tidal shearing effect. Consider the tidal torque of the central SBH at a distance r_{pc} in pc, where the Keplerian period is $t_K = 3 \times 10^4 M_{\bullet 7}^{-1/2} r_{\text{pc}}^{3/2} \text{ yr}$. To prevent a cloud with density $\rho = m_p n$ from shearing, it must be at least partially confined by its own gravity and/or the ambient magnetic field B . In the former case, the characteristic Jeans timescale is $t_J \sim (G\rho)^{-1/2} = 3 \times 10^4 n_7^{-1/2} \text{ yr}$,

where $n_7 = n/(10^7 \text{ cm}^{-3})$. Therefore, resistance to tidal shearing ($t_J < t_K$) sets a lower limit on the density of the cloud, leading to upper limits on its size R_c and mass M_{cl} :

$$n_7 > \frac{M_{\bullet,7}}{r_{\text{pc}}^3}, \quad R_c \lesssim 10^{16} \frac{N_{\text{H},23} r_{\text{pc}}^3}{M_{\bullet,7}} \text{ cm}, \quad M_{\text{cl}} \lesssim 7 \times 10^{-3} N_{\text{H},23} R_{c16}^2 M_{\odot} \quad (11)$$

where $R_{c16} = R_c/(10^{16} \text{ cm})$ and $N_{\text{H},23} = N_{\text{H}}/(10^{23} \text{ cm}^{-2})$. The resistance to tidal shearing does not guarantee confinement against the dispersive force of internal pressure. Self-gravity cannot confine these clouds because their low masses provide gravitational confinement only against internal motions with velocities $\lesssim 0.1 \text{ km s}^{-1}$. A corollary is that these clouds cannot collapse gravitationally to form stars. While self-gravity cannot hold a cloud together against dispersal, an external magnetic field $B \sim 1.5 \sigma_5 n_7^{1/2} \text{ mG}$ would suffice if the internal velocity dispersion is $\sigma_5 \times 1 \text{ km s}^{-1}$. Clouds with these very same properties can explain the masers detected in Circinus and NGC 3079, adding support to the suggestion that the outflow water masers are yet another manifestation of the dusty, molecular clouds that make up the torus region of the disk-wind. Densities of H_2O masers are frequently quoted as $\sim 10^8\text{--}10^9 \text{ cm}^{-3}$, but these are the optimal densities to produce the highest possible brightness from a single cloud. Because of the scaling properties of H_2O pumping (Elitzur et al., 1989), maser clouds with $n \sim 10^7 \text{ cm}^{-3}$ and $N_{\text{H}} \sim 10^{23} \text{ cm}^{-2}$ produce near-optimal inversion and detected radiation in cloud-cloud amplification. Proper motion measurements and comparisons of the disk and outflow masers offer a most promising means to probe the structure and motion of TOR clouds.

To produce a TOR with the required angular width, clouds must maintain a column density above $\sim 10^{21} \text{ cm}^{-2}$ during their rise to height $H \sim r$. If a cloud expands at the speed of sound c_s while rising with velocity v , then its size will increase by a factor $x \simeq 1 + (r/R_c)(c_s/v)$. We expect $c_s/v \simeq 10^{-2}$ since c_s is 1 km s^{-1} at a temperature of 100 K and the velocity scale of the cloud outflow is expected to be comparable to the Keplerian velocity, $v_K = 208 (M_{\bullet,7}/r_{\text{pc}})^{1/2} \text{ km s}^{-1}$. With $R_c/r \sim 10^{-3}$, the 3-D expansion of such a cloud during the rise to $H \sim r$ will cause its size to increase by a factor $x \sim 10$ and its column density ($\propto M_{\text{cl}}/R_c^2$) to decrease by a factor $x^2 \sim 100$, as required. Resistance to tidal shearing dictates that the density inside the cloud increase as $1/r^3$ as it gets closer to the central SBH (eq. 11). A cloud of a given density can exist only beyond a certain distance from the SBH; only denser clouds can survive at smaller radii, leading to a radially stratified structure. Similarly, the Keplerian velocity increases as $1/r^{1/2}$ as the SBH is approached. Typical BLR cloud densities and velocities, discussed elsewhere in these proceedings by H. Netzer, occur at $r \sim 10^{16}\text{--}10^{17} \text{ cm}$. It is possible that the BLR inner boundary occurs where the clouds can no longer overcome the SBH tidal shearing.

5.2 TOR Outflow—Properties and Consequences

The kinetic luminosity of the TOR outflow is $L_k^{\text{TOR}} = \int \frac{1}{2} M_{\text{cl}} v_{\text{cl}}^2 \cdot n_{\text{C}} v_{\text{cl}} dA$. The integration is over the disk area where TOR clouds are injected out of the plane with vertical velocity component v_{cl} . This injection velocity can be estimated from the dispersion velocity of molecular material in the disk — an outflow can be considered to have been established when the velocity of the ordered motion becomes comparable to that of the local random motions. From the maser observations in NGC 3079 Kondratko et al. (2005) find that the velocity dispersion in a small region ($\leq 5 \times 10^{16}$ cm) of strong emission is $\sim 14 \text{ km s}^{-1}$, which can be considered typical of the local random motions. Therefore, we parameterize the injection velocity as $v_{\text{cl}}(r) = 10 \text{ km s}^{-1} \times v_6(R_{\text{d}}) u(r)$, where $v_6(R_{\text{d}}) = v_{\text{cl}}(R_{\text{d}})/10 \text{ km s}^{-1}$ is expected to be of order unity and where $u = v(r)/v(R_{\text{d}})$. Without a full solution of the clumpy wind problem, which is far from becoming available, the dimensionless profile $u(r)$ of velocity variation across the disk plane remains unknown. However, it is quite certain that $u(r)$ decreases with r from its maximum of $u(R_{\text{d}}) = 1$; in particular, if the turbulent velocity is a fraction of the local Keplerian velocity then $u = (R_{\text{d}}/r)^{1/2}$. With $M_{\text{cl}} n_{\text{C}} = m_{\text{p}} N_{\text{H}} N_{\text{C}}$ and R_{d} from eq. 2 and taking $T_{\text{sub}} = 1500 \text{ K}$, the outflow kinetic luminosity is

$$L_k^{\text{TOR}} = 7 \times 10^{35} L_{45}^{1/2} N_{H,23}^{\text{tot}} v_6^3(R_{\text{d}}) \times I_3 \text{ erg s}^{-1}. \quad (12)$$

Here $N_{H,23}^{\text{tot}} = \mathcal{N}_0 N_{H,23}$ is the column density through all clouds in the outflow equatorial plane in units of 10^{23} cm^{-2} and $I_3 = \int_1^Y (u^3/y) dy \times Y/(Y-1)$ is an unknown dimensionless factor of order $\lesssim 1$. This result shows that the kinetic luminosity of the TOR cloud outflow is generally negligible in the overall energy budget of the AGN. This estimate for L_k^{TOR} does not lend support to the suggestion known as the “AGN–Galaxy connection” that outflows from the AGN may significantly affect the host galaxy. However, although the energy outflow is not a significant factor, the mass outflow is. A similar calculation for the mass outflow rate of TOR clouds yields

$$\dot{M}_{\text{out}}^{\text{TOR}} = 0.02 L_{45}^{1/2} N_{H,23}^{\text{tot}} v_6(R_{\text{d}}) \times I_1 M_{\odot} \text{ yr}^{-1} \quad (13)$$

where $I_1 = \int_1^Y (u/y) dy \times Y/(Y-1)$ is another unknown factor of order $\lesssim 1$. Since the clouds are likely imbedded in a continuous wind, the actual TOR outflow rate is probably somewhat higher. Steady-state mass conservation requires accretion into the TOR with a rate $\dot{M}_{\text{acc}}^{\text{TOR}} > \dot{M}_{\text{out}}^{\text{TOR}}$; if this constraint is not met, the TOR mass is depleted within a few Keplerian orbits (Elitzur & Shlosman, 2006). Mass accreted into the TOR and not injected into the outflow finds its way into the black hole, and is the fuel for the AGN luminosity. Therefore $\dot{M}_{\text{acc}}^{\text{TOR}} = \dot{M}_{\text{out}}^{\text{TOR}} + \dot{M}_{\text{acc}}^{\text{BH}}$, where $\dot{M}_{\text{acc}}^{\text{BH}}$ is the black hole

accretion rate, so $\dot{M}_{\text{acc}}^{\text{BH}} = \alpha \dot{M}_{\text{acc}}^{\text{TOR}}$ where $\alpha < 1$. In addition, $\dot{M}_{\text{acc}}^{\text{BH}}$ is related to the AGN bolometric luminosity via $L = \eta \dot{M}_{\text{acc}}^{\text{BH}} c^2$, where $\eta \sim 0.1$ is the gravitational conversion efficiency. We end up with $L = \epsilon \dot{M}_{\text{acc}}^{\text{TOR}} c^2$, where $\epsilon = \eta \alpha$, and the accretion into the TOR and the outflow away from it are related via

$$\frac{\dot{M}_{\text{out}}^{\text{TOR}}}{\dot{M}_{\text{acc}}^{\text{TOR}}} = \frac{\epsilon}{L_{45}^{1/2}} N_{H,23}^{\text{tot}} v_6(R_d) \times I_1. \quad (14)$$

This ratio cannot exceed unity, yet it increases when L decreases with all other factors remaining constant. Therefore, when the luminosity decreases the bound $\dot{M}_{\text{out}}^{\text{TOR}} < \dot{M}_{\text{acc}}^{\text{TOR}}$ is eventually violated, implying that the system cannot sustain the cloud outflow rate inferred from the TOR properties. The wind injection velocity $v_{\text{cl}}(R_d)$ is likely to change too when L decreases because the dust sublimation radius moves closer to the black hole (eq. 2), where all velocities become larger. As with any location in the accretion disk, the velocity scale of dynamic motions is determined by the local Keplerian velocity $v_{\text{K}}(R_d) = (GM_{\bullet}/R_d)^{1/2} \propto (L_{\text{Edd}}/L^{1/2})^{1/2}$. If we assume that $v_{\text{cl}}(R_d)$ is proportional to $v_{\text{K}}(R_d)$, eq. 14 becomes

$$\frac{\dot{M}_{\text{out}}^{\text{TOR}}}{\dot{M}_{\text{acc}}^{\text{TOR}}} = \frac{\epsilon'}{L_{45}^{1/4}} \left(\frac{L_{\text{Edd}}}{L} \right)^{1/2} N_{H,23}^{\text{tot}} \quad (15)$$

where the modified efficiency factor ϵ' absorbed all additional proportionality constants, including I_1 . At low accretion rates, the accretion may switch to a radiatively inefficient mode (RIAF; for recent reviews see Narayan, 2002; Yuan, 2007), namely, the efficiency ϵ' decreases too and we can expect the ratio $\epsilon'/L^{1/4}$ not to vary too much. The TOR equatorial column density must remain $N_{H,23}^{\text{tot}} \gtrsim 1$ as a definition of the AGN torus, to provide the optical depth required by the obscuration and observed IR emission. All in all, decreasing the luminosity at a fixed black-hole mass (L_{Edd}) causes an increase of $\dot{M}_{\text{out}}^{\text{TOR}}/\dot{M}_{\text{acc}}^{\text{TOR}}$, and when this ratio exceeds unity the TOR disappears. *The torus should disappear in low-luminosity AGN.* If we take $\epsilon \simeq 0.01$ and all other parameters ~ 1 in eq. 14, the torus disappearance should occur at bolometric luminosities below $\sim 10^{42} \text{ erg s}^{-1}$. Since the Eddington luminosity of a $10^7 M_{\odot}$ black-hole is $10^{45} \text{ erg s}^{-1}$, the torus disappearance can be expected at a typical Eddington ratio $L/L_{\text{Edd}} \sim 10^{-3}$.

5.3 The AGN Low-Luminosity End

A key prediction of the wind scenario is that the torus disappears at low bolometric luminosities ($\lesssim 10^{42} \text{ erg s}^{-1}$) because mass accretion can no longer

sustain the required cloud outflow rate, i.e., the large column densities. Observations seem to corroborate this prediction. In an HST study of a complete sample of low-luminosity ($\lesssim 10^{42}$ erg s $^{-1}$) FR I radio galaxies, Chiaberge et al. (1999) detected the compact core in 85% of sources. Since the radio selection is unbiased with respect to the AGN orientation, FR I sources should contain similar numbers of type 1 and type 2 objects, and Chiaberge et al suggested that the high detection rate of the central compact core implies the absence of an obscuring torus. This suggestion was corroborated by Whyson & Antonucci (2004) who demonstrated the absence of a dusty torus in M87, one of the sources in the FR I sample, by placing stringent limits on its thermal IR emission. Observations by Perlman et al. (2007) further solidified this conclusion. The IR radiation they detect in the M87 core comes primarily from non-thermal jet emission, with only a trace of thermal emission that is much weaker than what would be expected from an AGN torus and that can be attributed to neighboring dust. The behavior displayed by M87 appears to be common in FR I sources. Van der Wolk et al report in these proceedings the results of high resolution 12 μ m imaging observations of the nuclei of 27 radio galaxies, performed with the VISIR instrument on the VLT. The reported observations provide strong confirmation of the torus disappearance in FR I sources. They show that all the FR I objects in the sample lack dusty torus thermal emission, although they have non-thermal nuclei. Thermal dust emission was detected in about half the FR II nuclei, which generally have higher luminosities. In contrast, in almost all broad line radio galaxies in the sample the observations detected the thermal nucleus. Significantly, Ogle et al. (2007) find that most FR I and half of FR II sources have $L/L_{\text{Edd}} < 3 \cdot 10^{-3}$, while all sources with broad Balmer lines have $L/L_{\text{Edd}} > 3 \cdot 10^{-3}$.

The low-luminosities sources known as LINERs provide additional evidence for the torus disappearance. Maoz et al. (2005) conducted UV monitoring of LINERs with $L \lesssim 10^{42}$ erg s $^{-1}$ and detected variability in most of them. This demonstrates that the AGN makes a significant contribution to the UV radiation in each of the monitored sources and that it is relatively unobscured in all the observed LINERs, which included both type 1 and type 2. Furthermore, the histograms of UV colors of the type 1 and 2 LINERs show an overlap between the two populations, with the difference between the histogram peaks corresponding to dust obscuration in the type 2 objects of only ~ 1 magnitude in the R band. Such toroidal obscuration is minute in comparison with the torus obscuration in higher luminosity AGN. The predicted torus disappearance at low L does not imply that the cloud component of the disk wind is abruptly extinguished, only that its outflow rate is less than required by the IR emission observed in quasars and high-luminosity Seyferts. When $\dot{M}_{\text{out}}^{\text{TOR}}$ drops below these “standard” torus values, the outflow still provides toroidal obscuration as long as its column exceeds $\sim 10^{21}$ cm $^{-2}$. Indeed, Maoz et al find that some LINERs do have obscuration, but much smaller than “standard”. Line transmission through a low-obscuration torus might also explain the low

polarizations of broad H α lines observed by Barth et al. (1999) in some low luminosity systems.

If the toroidal obscuration were the only component removed from the system, all low luminosity AGN would become type 1 sources. In fact, among the LINERs monitored and found to be variable by Maoz et al there were both sources with broad H α wings (type 1) and those without (type 2). Since all objects are relatively unobscured, the broad line component is truly missing in the type 2 sources in this sample. Similarly, Panessa & Bassani (2002) note that the BLR is weak or absent in low luminosity AGN, and Laor (2003) presents arguments that some “true” type 2 sources, i.e., having no obscured BLR, do exist among AGNs with $L \lesssim 10^{42} \text{ erg s}^{-1}$. The absence of broad lines in these sources cannot be attributed to toroidal obscuration because their X-ray emission is largely unobscured. These findings have a simple explanation if when L decreases further beyond the disappearance of the TOR outflow, the suppression of mass outflow spreads radially inward from the disk’s dusty, molecular region into its atomic, ionized zone. Then the torus disappearance, i.e., removal of the toroidal obscuration by the dusty wind, would be followed by a diminished outflow from the inner ionized zone and disappearance of the BLR at some lower luminosity. Indeed, Ogle et al. (2007) find that all sources with broad Balmer lines have $L/L_{\text{Edd}} \gtrsim 3 \cdot 10^{-3}$, as noted above. Such an inward progression of the outflow turnoff as the accretion rate decreases can be expected naturally in the context of disk winds because mass outflow increases with the disk area. A diminished supply of accreted mass may suffice to support an outflow from the inner parts of the disk but not from the larger area of its outer regions. And with further decrease in inflow rate, even the smaller inner area cannot sustain the disk outflow. Since the accreted mass cannot be channeled in full into the central black hole, the system must find another channel for release of the excess accreted mass, and the only one remaining is the radio jets. Indeed, Ho (2002) finds that the AGN radio loudness $\mathcal{R} = L_{\text{radio}}/L_{\text{opt}}$ is *inversely* correlated with the mass accretion rate L/L_{Edd} , a correlation further verified by Greene, Ho, & Ulvestad (2006). This finding is supported by Sikora et al. (2007), who have greatly expanded this correlation and found an intriguing result: \mathcal{R} indeed increases inversely with L/L_{Edd} , but only so long as L/L_{Edd} remains $\gtrsim 10^{-3}$. At smaller accretion rates, which include all FR I radio galaxies, the radio loudness saturates and remains constant at $\mathcal{R} \sim 10^4$. This is precisely the expected behavior if as the outflow diminishes, the jets are fed an increasingly larger fraction of the accreted mass and finally, once the outflow is extinguished, all the inflowing material not funneled into the black hole is channeled into the jets, whose feeding thus saturates at a high conversion efficiency of accreted mass. It is important to note that radio loudness reflects the relative contribution of radio to the overall radiative emission; a source can be radio loud even at a low level of radio emission if its overall luminosity is small, and vice versa.

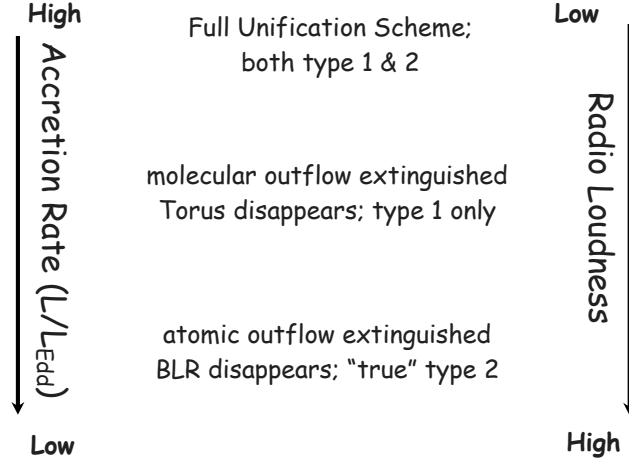


Fig. 12. Conjectured scheme for AGN evolution with decreasing accretion rate.

The evolutionary scheme just outlined is sketched in figure 12. A similar anti-correlation between radio loudness and accretion rate exists also in X-ray binaries. These sources display switches between radio quiet states of high X-ray emission and radio loud states with low X-ray emission (Fender et al., 2004). While in X-ray binaries this behavior can be followed with time in a given source, in AGN it is only manifested statistically. Comparative studies of AGN and X-ray binaries seem to be a most useful avenue to pursue.

5.4 Limitations

The scheme just outlined was not derived from a detailed dynamical model for clumpy disk outflow in AGN. Such models do not yet exist. Instead, the results follow from considerations of basic conservation laws within the framework of the wind paradigm for the AGN torus. The conclusion that the TOR should disappear at low accretion rates is almost unavoidable because the outflow rate decreases more slowly than does the luminosity. In eq. 14, our ignorance of all dynamics details is lumped into the efficiency factor ϵ . Although this factor is largely unknown, the torus disappearance conclusion would be off only if ϵ varied with luminosity in a way that completely offset the explicit L -dependencies in eqs. 14 and 15. Observations indicate that this is not the case. The most recent review by Ho (2008) presents extensive observational evidence for the disappearance of the torus and the BLR in low luminosity AGN.

The lack of explicit dynamics model is both the weakness and strength of the presented arguments. Our results provide constraints that have to be met by any detailed model constructed to explain the AGN torus within the disk wind paradigm. It should be noted that we were able to estimate only the properties of the TOR outflow and deduce that this outflow must be turned

off at low luminosities. The BLR disappearance is then deduced from the observational evidence that the low luminosity AGN do not become exclusively type 1 objects. A possible dynamical explanation is offered by Nicastro (2000), whose work on the role of radiation pressure provides the earliest prediction for BLR disappearance at low L/L_{Edd} .

5.5 Final Speculations

While outflow considerations set limits on the AGN low luminosity end, they do not provide any constraints on the TOR at high luminosities. From observations, the fraction f_2 of obscured AGN decreases with bolometric luminosity (see sec. 3.2). As is evident from figure 11, this can be produced by either a decrease of σ at constant \mathcal{N}_0 or a decrease of \mathcal{N}_0 at constant σ . The torus radial dimensions are set from its inner radius R_d , which increases with L due to dust sublimation (eq. 2). Therefore, the decreasing- σ option would arise if the TOR height were independent of luminosity or increased more slowly than $L^{1/2}$, the decreasing- \mathcal{N}_0 option would arise if the TOR outer radius were independent of luminosity or increased more slowly than $L^{1/2}$. The outflow outer radius is plausibly confined to within the SBH gravitational influence radius, $R_o < 35 \text{ pc} \times (M_{\bullet,7}/\Omega_1^2)^{1/3}$ (sec. 5). As noted in sec. 3.3, an upper bound on the torus outer radius set conservatively from IR observations is $R_o < 12 L_{45}^{1/2} \text{ pc}$. So whenever $L_{45} \gtrsim 9(M_{\bullet,7}/\Omega_1^2)^{2/3}$, the TOR outflow is cut at an outer radius smaller than that containing the typical number of clouds according to IR observations, providing a possible explanation for the decreasing- \mathcal{N}_0 option.

Finally, the AGN bolometric luminosity implies accretion into the black hole at the rate $\dot{M}_{\text{acc}}^{\text{BH}} \sim 0.1 L_{45} M_{\odot} \text{ yr}^{-1}$, assuming radiation efficiency $\eta \sim 0.1$ (see sec. 5.2). The AGN phase lasts probably $\sim 10^7$ – 10^8 years, thus the overall mass accreted is $\sim 10^6$ – $10^7 L_{45} M_{\odot}$. Since Seyfert luminosities do not exceed $\sim 10^{45} \text{ erg s}^{-1}$ at most, the entire mass they typically accrete from the host galaxy during an AGN episode is no more than that contained in a single giant molecular cloud. In contrast, QSO luminosities reach upward of $10^{48} \text{ erg s}^{-1}$. If QSO lifetimes are similar, the mass fed into the SBH is comparable to that of an entire galaxy. This suggests that the quasar and Seyfert nuclear activities could be triggered differently. Starting a quasar might require interaction with another galaxy to trigger accretion of the prodigious amounts of fuel that can only be supplied by a full galactic mass. In contrast, a Seyfert episode may represent the occasional capture of a giant molecular cloud by the SBH that is now known to exist at the center of most galaxies.

6 Concluding Remarks

The clumpy nature of the obscuring torus, long ago deduced from theoretical considerations and now being verified by observations, dictates a fundamental change in the approach to some basic issues regarding AGN. Foremost among them is analysis of the type 1 and type 2 source statistics. Because the viewing angle determines the obscuration only in the sense of probability, and not absolutely, translating source statistics into torus parameters becomes a difficult task. In addition to the torus angular width σ , which has been used as the sole parameter of such analysis, it involves also the mean number of clouds \mathcal{N}_0 , making it impossible to determine both of them from the single measured quantity f_2 . In particular, the observed decrease of f_2 with increasing luminosity can be attributed to a decrease of either σ or \mathcal{N}_0 or both. Meaningful constraints on the torus physical properties can be placed only through combination of different types of data. Comparisons of UV/optical and X-ray properties in individual sources and in samples offer especially promising analysis modes for deducing detailed torus properties.

The low-luminosity end of AGN offers a rich variety of interesting phenomena. The consecutive disappearances of the torus and the BLR at low luminosities, or low Eddington ratios, and the simultaneous increase in radio loudness fit naturally into the outflow paradigm for the AGN torus. Detailed observational and theoretical studies of these phenomena would enhance significantly our understanding of the black-hole environment.

Acknowledgements: Discussions with numerous colleagues were instrumental in formulating many of the ideas presented here. Special thanks to Roberto Maiolino, who pointed out the important role of the Eddington ratio described in sec. 5.2, Ari Laor and Isaac Shlosman. Partial support by NSF and NASA is gratefully acknowledged.

References

- Alonso-Herrero, A., Quillen, A. C., Rieke, G. H., Ivanov, V. D., & Efstathiou, A. 2003, *AJ*, 126, 81
- Aretxaga, I., Jørguet, B., Kunth, D., Melnick, J., & Terlevich, R. J. 1999, *ApJ*, 519, L123
- Barth, A. J., Filippenko, A. V., & Moran, E. C. 1999, *ApJ*, 525, 673
- Bassani, L., Dadina, M., Maiolino, R., et al. 1999, *ApJS*, 121, 473
- Blandford, R. D. & Payne, D. G. 1982, *MNRAS*, 199, 883
- Bottorff, M., Korista, K. T., Shlosman, I., & Blandford, R. D. 1997, *ApJ*, 479, 200
- Bottorff, M. C., Korista, K. T., & Shlosman, I. 2000, *ApJ*, 537, 134

Braito, V., Della Ceca, R., Piconcelli, E., et al. 2004, *A&A*, 420, 79
 Buchanan, C. L., Gallimore, J. F., O’Dea, C. P., et al. 2006, *AJ*, 132, 401
 Chiaberge, M., Capetti, A., & Celotti, A. 1999, *A&A*, 349, 77
 Conway, J., Elitzur, M., & Parra, R. 2005, *Ap&SS*, 295, 319
 Conway, J., Elitzur, M., & Parra, R. 2008, in preparation
 Crenshaw, D. M. & Kraemer, S. B. 2000, *ApJ*, 532, L101
 Draine, B. T. 2003, *ApJ*, 598, 1017
 Eckart, M. E., Stern, D., Helfand, D. J., et al. 2006, *ApJS*, 165, 19
 Efstathiou, A. & Rowan-Robinson, M. 1994, *MNRAS*, 266, 212
 Elitzur, M., Hollenbach, D. J., & McKee, C. F. 1989, *ApJ*, 346, 983
 Elitzur, M. & Shlosman, I. 2006, *ApJ*, 648, L101
 Elvis, M. 2004, in *ASP Conf. Ser. 311: AGN Physics with the Sloan Digital Sky Survey*, ed. G. T. Richards & P. B. Hall, 109
 Elvis, M., Risaliti, G., Nicastro, F., et al. 2004, *ApJ*, 615, L25
 Emmering, R. T., Blandford, R. D., & Shlosman, I. 1992, *ApJ*, 385, 460
 Eracleous, M. 2004, in *ASP Conf. Ser. 311: AGN Physics with the Sloan Digital Sky Survey*, ed. G. T. Richards & P. B. Hall, 183
 Everett, J. E. 2005, *ApJ*, 631, 689
 Fender, R. P., Belloni, T. M., & Gallo, E. 2004, *MNRAS*, 355, 1105
 Fritz, J., Franceschini, A., & Hatziminaoglou, E. 2006, *MNRAS*, 366, 767
 Gallagher, S. C., Brandt, W. N., Chartas, G., et al. 2006, *ApJ*, 644, 709
 Gallagher, S. C. & Everett, J. E. 2007, in *ASP Conf. Ser. 373: The Central Engine of Active Galactic Nuclei*, ed. L. C. Ho & J.-M. Wang, 305–314
 Galliano, E., Alloin, D., Granato, G. L., & Villar-Martín, M. 2003, *A&A*, 412, 615
 Gallimore, J. F., Henkel, C., Baum, S. A., et al. 2001, *ApJ*, 556, 694
 Garcet, O., Gandhi, P., Gosset, E., et al. 2007, *A&A*, 474, 473
 George, I. M., Turner, T. J., Netzer, H., et al. 1998, *ApJS*, 114, 73
 Granato, G. L. & Danese, L. 1994, *MNRAS*, 268, 235
 Granato, G. L., Danese, L., & Franceschini, A. 1997, *ApJ*, 486, 147
 Gratadour, D., Clénet, Y., Rouan, D., Lai, O., & Forveille, T. 2003, *A&A*, 411, 335
 Greene, J. E., Ho, L. C., & Ulvestad, J. S. 2006, *ApJ*, 636, 56
 Greenhill, L. J. 2005, in *ASP Conf. Ser. 340: Future Directions in High Resolution Astronomy*, ed. J. Romney & M. Reid, 203
 Greenhill, L. J., Booth, R. S., Ellingsen, S. P., et al. 2003, *ApJ*, 590, 162
 Greenhill, L. J. & Gwinn, C. R. 1997, *Ap&SS*, 248, 261
 Guainazzi, M., Fiore, F., Matt, G., & Perola, G. C. 2001, *MNRAS*, 327, 323
 Guainazzi, M., Matt, G., & Perola, G. C. 2005, *A&A*, 444, 119
 Hall, P. B., Hutsemékers, D., Anderson, S. F., et al. 2003, *ApJ*, 593, 189
 Hao, L., Strauss, M. A., Fan, X., et al. 2005, *AJ*, 129, 1795
 Hao, L., Weedman, D. W., Spoon, H. W. W., et al. 2007, *ApJ*, 655, L77
 Ho, L. C. 2002, *ApJ*, 564, 120
 Ho, L. C. 2008, *ARA&A*, in press (arXiv0803.2268)
 Horst, H., Smette, A., Gandhi, P., & Duschl, W. J. 2006, *A&A*, 457, L17

- Ivezić, Ž. & Elitzur, M. 1997, *MNRAS*, 287, 799
- Jaffe, W., Meisenheimer, K., Röttgering, H. J. A., et al. 2004, *Nature*, 429, 47
- Kartje, J. F. & Königl, A. 1996, *Vistas in Astronomy*, 40, 133
- Kartje, J. F., Königl, A., & Elitzur, M. 1999, *ApJ*, 513, 180
- Kinney, A. L., Schmitt, H. R., Clarke, C. J., et al. 2000, *ApJ*, 537, 152
- Kondratko, P. T., Greenhill, L. J., & Moran, J. M. 2005, *ApJ*, 618, 618
- Königl, A. & Kartje, J. F. 1994, *ApJ*, 434, 446
- Krolik, J. H. & Begelman, M. C. 1988, *ApJ*, 329, 702
- Krolik, J. H., Madau, P., & Zycki, P. T. 1994, *ApJ*, 420, L57
- Laor, A. 2003, *ApJ*, 590, 86
- Levenson, N. A., Krolik, J. H., Życki, P. T., et al. 2002, *ApJ*, 573, L81
- Levenson, N. A., Sirocky, M. M., Hao, L., et al. 2007, *ApJ*, 654, L45
- Lutz, D., Maiolino, R., Spoon, H. W. W., & Moorwood, A. F. M. 2004, *A&A*, 418, 465
- Maccararo, T., Perola, G. C., & Elvis, M. 1982, *ApJ*, 257, 47
- Maiolino, R., Marconi, A., Salvati, M., et al. 2001, *A&A*, 365, 28
- Maiolino, R., Shemmer, O., Imanishi, M., et al. 2007, *A&A*, 468, 979
- Maoz, D., Nagar, N. M., Falcke, H., & Wilson, A. S. 2005, *ApJ*, 625, 699
- Mason, R. E., Geballe, T. R., Packham, C., et al. 2006, *ApJ*, 640, 612
- Mathis, J. S., Ruml, W., & Nordsieck, K. H. 1977, *ApJ*, 217, 425
- Nandra, K. & Pounds, K. A. 1994, *MNRAS*, 268, 405
- Narayan, R. 2002, in *Lighthouses of the Universe: The Most Luminous Celestial Objects and Their Use for Cosmology*, ed. M. Gilfanov, R. Sunyaev, & E. Churazov, 405
- Natta, A. & Panagia, N. 1984, *ApJ*, 287, 228
- Nenkova, M., Ivezić, Ž., & Elitzur, M. 2002, *ApJ*, 570, L9
- Nenkova, M., Sirocky, M. M., Ivezić, Ž., & Elitzur, M. 2008a, *ApJ*, submitted
- Nenkova, M., Sirocky, M. M., Nikutta, R., Ivezić, Ž., & Elitzur, M. 2008b, *ApJ*, submitted
- Netzer, H. & Laor, A. 1993, *ApJ*, 404, L51
- Nicastro, F. 2000, *ApJ*, 530, L65
- Ogle, P. M., Antonucci, R. R. J., & Whysong, D. 2007, in *ASP Conf. Ser. 373: The Central Engine of Active Galactic Nuclei*, ed. L. C. Ho & J.-M. Wang, 578–581
- Ossenkopf, V., Henning, T., & Mathis, J. S. 1992, *A&A*, 261, 567
- Packham, C., Young, S., Fisher, S., et al. 2007, *ApJ*, 661, L29
- Page, M. J., Loaring, N. S., Dwelly, T., et al. 2006, *MNRAS*, 369, 156
- Panessa, F. & Bassani, L. 2002, *A&A*, 394, 435
- Perlman, E. S., Mason, R. E., Packham, C., et al. 2007, *ApJ*, 663, 808
- Perola, G. C., Puccetti, S., Fiore, F., et al. 2004, *A&A*, 421, 491
- Pier, E. A. & Krolik, J. H. 1992, *ApJ*, 401, 99
- Pier, E. A. & Krolik, J. H. 1993, *ApJ*, 418, 673
- Risaliti, G., Elvis, M., Fabbiano, G., et al. 2007, *ApJ*, 659, L111
- Risaliti, G., Elvis, M., & Nicastro, F. 2002, *ApJ*, 571, 234

- Risaliti, G., Maiolino, R., & Salvati, M. 1999, *ApJ*, 522, 157
- Schinnerer, E., Eckart, A., Tacconi, L. J., Genzel, R., & Downes, D. 2000, *ApJ*, 533, 850
- Schmitt, H. R., Antonucci, R. R. J., Ulvestad, J. S., et al. 2001, *ApJ*, 555, 663
- Schmitt, H. R., Pringle, J. E., Clarke, C. J., & Kinney, A. L. 2002, *ApJ*, 575, 150
- Severgnini, P., Caccianiga, A., Braitto, V., et al. 2003, *A&A*, 406, 483
- Shlosman, I., Begelman, M. C., & Frank, J. 1990, *Nature*, 345, 679
- Sikora, M., Stawarz, L., & Lasota, J.-P. 2007, *ApJ*, 658, 815
- Silva, L., Maiolino, R., & Granato, G. L. 2004, *MNRAS*, 355, 973
- Silverman, J. D., Green, P. J., Barkhouse, W. A., et al. 2005, *ApJ*, 618, 123
- Simpson, C. 2005, *MNRAS*, 360, 565
- Sirocky, M. M., Levenson, N. A., Elitzur, M., Spoon, H. W. W., & Armus, L. 2008, *ApJ*, 678, 729
- Smith, D. A. & Done, C. 1996, *MNRAS*, 280, 355
- Sofue, Y., Tutui, Y., Honma, M., et al. 1999, *ApJ*, 523, 136
- Sparke, L. S. & Gallagher, III, J. S. 2006, *Galaxies in the Universe*, 2nd Edition (Cambridge University Press)
- Spoon, H. W. W., Marshall, J. A., Houck, J. R., et al. 2007, *ApJ*, 654, L49
- Sturm, E., Hasinger, G., Lehmann, I., et al. 2006, *ApJ*, 642, 81
- Suganuma, M., Yoshii, Y., Kobayashi, Y., et al. 2006, *ApJ*, 639, 46
- Tristram, K. R. W., Meisenheimer, K., Jaffe, W., et al. 2007, *A&A*, 474, 837
- Turner, T. J., George, I. M., Nandra, K., & Mushotzky, R. F. 1997a, *ApJS*, 113, 23
- Turner, T. J., George, I. M., Nandra, K., & Mushotzky, R. F. 1997b, *ApJ*, 488, 164
- Urry, C. M. & Padovani, P. 1995, *PASP*, 107, 803
- Weigelt, G., Wittkowski, M., Balega, Y. Y., et al. 2004, *A&A*, 425, 77
- Whysong, D. & Antonucci, R. 2004, *ApJ*, 602, 116
- Wolf, S. 2003, *ApJ*, 582, 859
- Yuan, F. 2007, in *ASP Conf. Ser. 373: The Central Engine of Active Galactic Nuclei*, ed. L. C. Ho & J.-W. Wang, 95